Quaternary Geochronology 54 (2019) 101006

A multi-dating approach to age-modelling long continental records: The 135 ka El Cañizar de Villarquemado sequence (NE Spain)

B.L. Valero-Garcés[a,b,*], P. González-Sampériz[a], G. Gil-Romera[a,c], B.M. Benito[d], A. Moreno[a,b], B. Oliva-Urcia[e], J. Aranbarri[f], E. García-Prieto[a], M. Frugone[g,b], M. Morellón[h,m], L.J. Arnold[i], M. Demuro[i], M. Hardiman[j], S.P.E. Blockley[k], C.S. Lane[l]

a Pyrenean Institute of Ecology (IPE) – CSIC, Avda Montañana 1005, E-50059 Zaragoza, Spain

b Laboratorio Internacional de Cambio Global, CSIC, PUC, UFRJ, Avda Montañana 1005, E-50059, Zaragoza, Spain

c Department of Geography and Environmental Sciences, Llandinam Building, Penglais Campus, Aberystwyth University, SY233DB, Aberystwyth, United Kingdom

d Ecological and Environmental Change Research Group, Department of Biological Sciences, University of Bergen, Norway

e Department of Geology and Geochemistry, Faculty of Sciences, Universidad Autónoma de Madrid, C/ Francisco Tomás y Valiente 7. Campus de Cantoblanco, E-28049, Madrid, Spain

f Department of Geography, Prehistory and Archaeology, University of the Basque Country, Francisco Tomás y Valiente, s/n, E-01006, Vitoria-Gasteiz, Spain

g Department of Ecology, Pontificia Universidad Católica de Chile, Avda. Alameda, Santiago, Chile

h CITIMAC, University of Cantabria, Avenida de los Castros s/n, E-39005 Santander, Cantabria, Spain

i School of Physical Sciences, Environment Institute, Institute for Photonics and Advanced Sensing (IPAS), University of Adelaide, North Terrace Campus, Adelaide, SA, 5005, Australia

j Department of Geography, University of Portsmouth, Portsmouth, PO1 3HE, UK

k Centre for Quaternary Research, Department of Geography, Royal Holloway, University of London, Egham, Surrey, TW2 0SE, UK

l Department of Geography, University of Cambridge, Downing Place, Cambridge, CB2 3EN, UK

m Departamento de Geodinámica, Estratigrafía y Paleontología, Facultad de Ciencias Geológicas, Universidad Complutense de Madrid, 28040 Madrid, Spain

* Corresponding author. Pyrenean Institute of Ecology (IPE) – CSIC, Avda Montañana 1005. E-50059 Zaragoza, Spain. E-mail address: blas@ipe.csic.es (B.L. Valero-Garcés).
https://doi.org/10.1016/j.quageo.2019.101006

Keywords:

Bayesian age model Radiocarbon OSL IRSL Last glacial cycle Mediterranean Continental sequences

ABSTRACT

We present a multidisciplinary dating approach -including radiocarbon, Uranium/Thorium series (U/Th), paleomagnetism, single-grain optically stimulated luminescence (OSL), polymineral fine-grain infrared stimulated luminescence (IRSL) and tephrochronology -used for the development of an age model for the Cañizar de Villarquemado sequence (VIL) for the last ca. 135 ka. We describe the protocols used for each technique and discuss the positive and negative results, as well as their implications for interpreting the VIL sequence and for dating similar terrestrial records. In spite of the negative results of some techniques, particularly due to the absence of adequate sample material or insufficient analytical precision, the multi-technique strategy employed here is essential to maximize the chances of obtaining robust age models in terrestrial sequences. The final Bayesian age model for VIL sequence includes 16 AMS ^{14}C ages, 9 single-grain quartz OSL ages and 5 previously published polymineral fine-grain IRSL ages, and the accuracy and resolution of the model are improved by incorporating information related to changes in accumulation rate, as revealed by detailed sedimentological analyses. The main paleohydrological and vegetation changes in the sequence are coherent with global Marine Isotope Stage (MIS) 6 to 1 transitions since the penultimate Termination, although some regional idiosyncrasies are evident, such as higher moisture variability than expected, an abrupt inception of the last glacial cycle and a resilient response of vegetation in Mediterranean continental Iberia in both Terminations.

1. Introduction

Major advances in paleoclimate research have been made possible only after improving numerical dating methods, reducing the time uncertainties of reconstructed changes and consequently facilitating our ability to precisely compare ice, marine and terrestrial records along spatial and temporal transects. Only with independent and robust age models we can test ‘leads’ and ‘lags’ in teleconnections between the atmospheric, marine, terrestrial and cryospheric realms (Hoek et al., 2008) and understand spatial patterns and mechanisms behind abrupt climate fluctuations, such as those documented within the last glacial cycles (Broecker, 2000).

During the last decades, the scientific community has made a significant effort to recover new, long continental sequences, extending beyond the last glacial cycle from classical sites such as Grande Pile (Woillard, 1978), Les Echets (de Beaulieu and Reille, 1989), Velay (Reille et al., 2000), Monticchio (Allen and Huntley, 2009), Ioannina (Tzedakis et al., 2003), or Tenaghi Philippon (Tzedakis et al., 2006). Several outstanding long sequences have been obtained thanks to international initiatives such as the International Continental Scientific Drilling Program (ICDP, https://www.icdp-online.org/home/) (e.g., Lake Titicaca (Fritz et al., 2007), Potrok Aike (Zolitschka et al., 2013), Dead Sea (Stein et al., 2011), Lake Van (Litt et al., 2009), Petén Itzá (Hodell et al., 2008), El'gygytgyn (Melles et al., 2012), Lake Ohrid (Lézine et al., 2010; Zanchetta et al., 2016), Lake Chalco (Brown et al., 2012), Lake Junin (Rodbell and Abbott, 2012), and Towuti in Indonesia (Russell et al., 2016). These long sequences span several glacial cycles and contain a detailed history of changes in vegetation, environmental and climate. However, in all cases, obtaining a robust chronology has remained a challenge. The exceptions to this rule are the long, continuous, annually laminated terrestrial records able to produce absolute and independent varve chronologies, such as Lake Suigetsu in central Japan for the last 70,000 years (Ojala et al., 2012) or well-dated speleothems that accurately cover long time periods, sometimes with excellent resolution (Wang et al., 2001; Pérez-Mejías et al., 2017). Unfortunately, these records are not common.

Due to the difficulties of obtaining independent, numerical, reliable and robust chronologies, most of the well-known long traditional sequences rely on either directly or indirectly tuning to orbital configurations or ice core chronologies (Tzedakis et al., 2006; Blaauw, 2012). This tuning approach precludes the correct identification of either regional and local particularities or potential leads and lags on different spatial and chronological scales (Brauer et al., 2007).

A combination of different dating techniques, depending on the age and type of material, is commonly applied to resolve the timing of past events in long terrestrial sequences. Radiocarbon dating is the most commonly used for the last 50,000 years (50 ka), although longer calibration curves have become available during the last few decades (Reimer et al., 2004, 2009, 2013). Uncertainties of more than several hundred years are frequent, particularly beyond the Last Glacial Maximum (LGM). Another common limitation of radiocarbon dating in terrestrial sequences is the infrequent preservation of terrestrial organic remains suitable for dating, particularly in semi-arid areas, as well as the occurrence of reworking processes (González-Sampériz et al., 2008; Valero-Garcés and Moreno, 2011; Lionello et al., 2012). U/Th series dating, commonly applied to speleothems, provides higher precision and longer time scales and it has been also used in lacustrine sequences (Placzek et al., 2006a) but its applicability depends on the presence of highly pure endogenic carbonate in the lacustrine sediments (Bischoff and Cummins, 2001; Placzek et al., 2006a, b). Paleomagnetic dating based on geomagnetic excursions, inclination and/or declination changes requires a minimum amount of ferromagnetic minerals carrying a primary (i.e. acquired at the time of sedimentation) magnetic signal that clearly defines the paleomagnetic characteristic components along the sequence (Roberts, 2008). For measurements of declination, methods are needed to precisely record the original orientation of sampled sediments, and the geographic location is also important for some magnetic properties. Tephras can provide punctuated, numerical, highly accurate ages (e.g., Zanchetta et al., 2011), but discrete ash-layers are not always preserved in terrestrial settings and even cryptotephras are sometimes difficult to detect in lacustrine sediments (Davies, 2015). Despite improvements in the identification and analysis of microscopic volcanic ash layers and cryptotephras transported across very long distances (Blockley et al., 2005; Lane et al., 2017), the use of this technique is spatially limited to regions where material derived eruptions was deposited and preserved. Tephra layers may serve as precise markers even when the age is unknown and the use of this technique can be extended to fingerprinting tephra of unknown source but distinctive geochemistry to correlate across regions. Luminescence dating techniques such as optically stimulated luminescence (OSL) of quartz and infrared stimulated luminescence (IRSL) of feldspars only require a relatively small amount of siliciclastic material to determine the burial age of terrestrial sediment sequences (the last time since sunlight exposure). However, in spite of recent developments (e.g., single-grain techniques or extended-range approaches; Murray and Roberts, 1997; Arnold et al., 2015), the suitability of luminescence dating techniques may be compromised by certain depositional or post-depositional complications (e.g., incomplete resetting of residual signals prior to burial or post-depositional mixing; Arnold et al., 2008; Arnold and Roberts, 2009) and the analytical precision of these techniques (typically > 5% at 1σ; e.g., Arnold and Demuro, 2018)is sometimes sub-optimal for high-resolution studies (e.g., Fu et al., 2017; De Deckker et al., 2019).

In summary, most of the available dating methods in terrestrial sequences require certain amounts of specific sediment components and it is unlikely that a single technique can provide a universally robust, high-resolution chronology. These various techniques do not necessarily date the same events and so it is critical to discuss the relevant sedimentological and stratigraphic relationships when comparing ages generated by different techniques. Additionally, a unique problem of long terrestrial records such as lacustrine sequences compared to marine or speleothem records is the larger temporal and spatial variability of sedimentary facies and depositional environments (Cohen, 2003). Within the same sedimentary basin and in the same site, even when located at the deepest part of the basin, depositional dynamics could have greatly changed during the last glacial cycles and sedimentation rates sometimes vary by several orders of magnitude. Thus, linear extrapolation of sedimentation rates without considering these changes in sedimentary facies produces age models with large uncertainties.

In this paper we summarize the efforts to directly date and construct a robust age model for a long lacustrine sequence from Southwestern Europe: El Cañizar de Villarquemado paleolake (hereafter referred as VIL). The Iberian Peninsula constitutes a sensitive area to reconstruct past hydrological changes (Giorgi and Lionello, 2008; García-Ruiz et al., 2011; Valero-Garcés and Moreno, 2011 and references therein; Morellón et al., 2018) and due to its particular location, with the influence of mid latitude and sub-tropical forcings and a strong Mediterranean – Atlantic climatic gradient, it is a unique place to study the interplay of atmospheric patterns during the last glacial cycles (Lionello et al., 2012; Tzedakis, 2007) and their environmental impacts on the continents through the Late Quaternary (e.g., Carrión and Leroy, 2010 and references therein; Magri et al., 2017). Previous research has demonstrated the potential of this site as a recorder of hydrological and vegetation changes in semi-arid continental regions of the Iberian Peninsula during the last ca. 120–130 ka (Moreno et al., 2012; González-Sampériz et al., 2013; Aranbarri et al., 2014; García-Prieto, 2015). VIL sequence (Fig. 1) extends back to Termination II and thus, constitutes a reference site for Southern Europe paleoclimate and paleoenvironmental variations covering the last two glacial cycles. Here we present and discuss the multidisciplinary dating approach (including radiocarbon, U/Th, paleomagnetism, single-grain quartz OSL, polymineral fine-grain IRSL and tephrochronology) used for the development of the best possible age model for the VIL sequence over the last ca. 135 ka, and discuss the main benchmarks used to produce such a model that might be useful for other similar long sequences. We explore the coherence of this age model against the available sedimentological data, preliminary selected pollen results, and other records from mid-latitudes.

2. Regional setting

2.1. The Jiloca Basin

The ‘El Cañizar de Villarquemado’ wetland is located in the Iberian Range, Northeastern Spain (Fig. 1A), at ca. 1000 m a.s.l., in the southernmost area of the 60 km long Jiloca Depression, an Upper Pliocene N-S half-graben bounded by NW-SE trending normal faults (Rubio and Simon, 2007). During the Quaternary, the northern areas of the Jiloca Basin changed to exorheic drainage progressively while in the southern area endorheic conditions remained (Gutiérrez-Elorza and Gracia, 1997) and a shallow (up to 2.8 m deep) lake developed, covering a maximum surface area of 11.3 km2 (Fig. 1B) and becoming the largest freshwater lake in the Iberian Range and one of the largest in the Iberian Peninsula (Rubio, 2004). The lake was drained to the north during the 18th century to increase agricultural land and reduce flooded areas perceived as a source of mosquito-borne diseases (Rubio, 2004). The evolution of the lake basin has been controlled by tectonics, subsidence, and the depositional dynamics of two ephemeral streams to the north, the Villarrosano and Rebollos. As the basin sits on Mesozoic limestones, variable karstic activity during the last millennia could also have affected base level and influenced depositional history (Gracia et al., 2003; Gutiérrez et al., 2008, 2012).

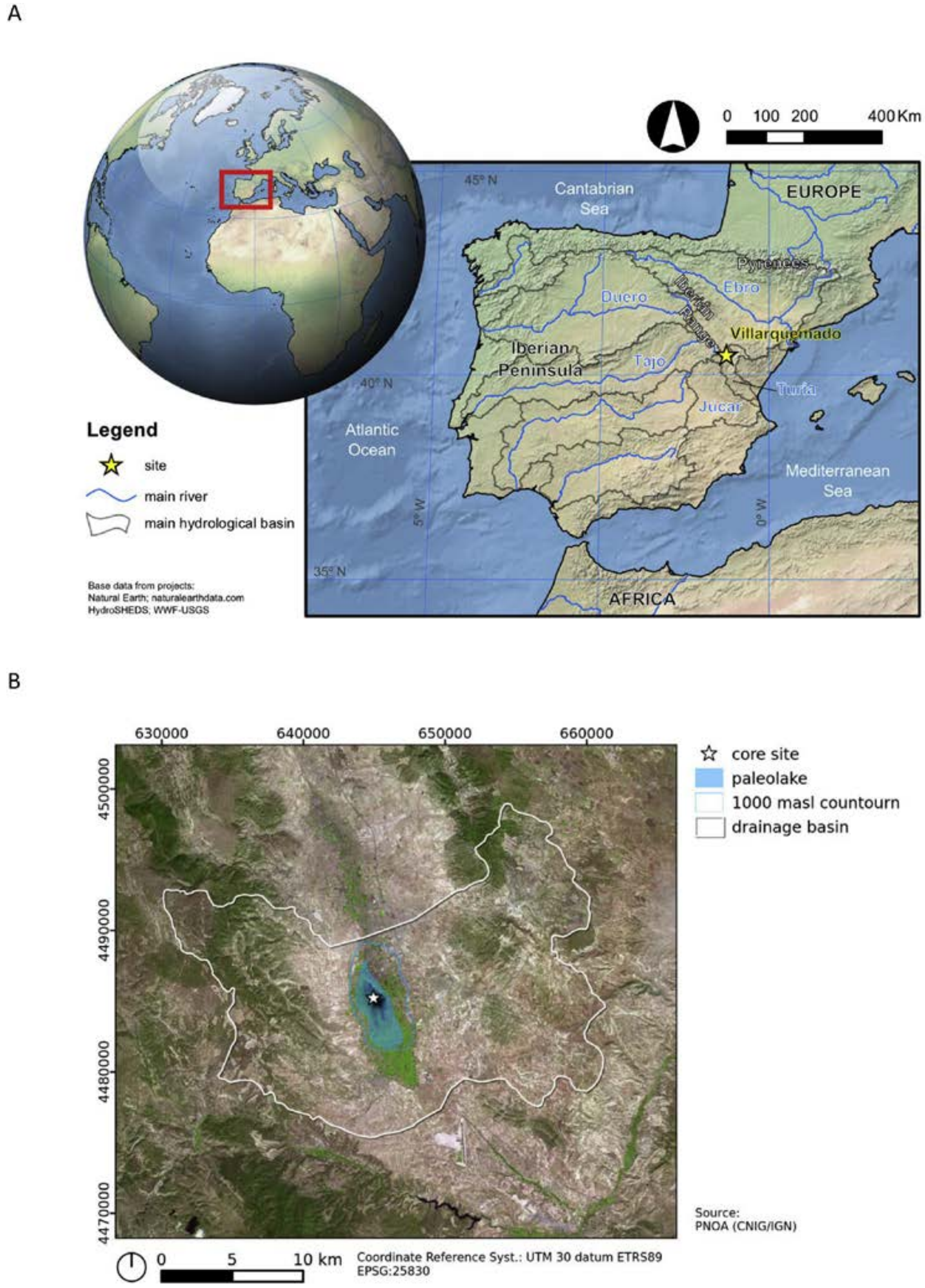

Fig. 1. A. Location of Cañizar de Villarquemado Basin. B. Map of the watershed and maximum surface area of the wetland prior to drainage.

Current regional vegetation plant communities are mainly composed by oaks (*Quercus ilex rotundifolia, Q. faginea*), junipers (*Juniperus thurifera, J. phoenicea*), and pines (*Pinus nigra, P. pinaster* and *P. sylvestris*) as the dominant trees, depending on altitude, exposure and soil type. Open

Mediterranean xerophytic shrub communities with *Rhamnus alaternus, Genista scorpius, Ephedra fragilis, Thymus* spp., *Rosmarinus officinalis* and *Artemisia assoana* amongst others are also frequent. The wetland surroundings are mostly cultivars. The climate of the region is Continental Mediterranean with long cold winters, hot summers, and a large water deficit (Lopez-Martín et al., 2007).

2.2. The Cañizar de Villarquemado sediment (VIL) sequence

After an exploratory Livingstone extraction of ca. 2 m core length (VIL05-1A-1L), a 74 m long core was recovered in 2005 with a truck–mounted drill rig in the central area of the wetland (VIL05-1B1T), where the basin depocenter was located (987 m a.s.l, 40°30'N; 1°18'W). The sediment cores were split lengthwise in two halves and imaged with a GEOTEK camera. High-resolution magnetic susceptibility profiles were acquired with a GEOTEK multisensory core data logger at the Limnological Research Center, University of Minnesota. Total Organic Carbon (TOC), Total Inorganic Carbon (TIC) and Total Nitrogen (TN) measurement were performed in samples taken at 2 cm intervals. XRF scanner measurements were performed every 4 cm with the ITRAX XRF at the Large Lakes Observatory, University of Minnesota. Cores were correlated based on key markers, facies and geochemical profiles.

Twenty facies were identified and described based on sediment composition, textures, color and microscopic observations of smear slides following Schnurrenberger et al. (2003). They correspond to four textural types (sand, coarse silt, fine silt, organic-rich) (Table 1 and Fig. 2) and have been grouped in four facies associations (FA) and their interpreted depositional environments: carbonate lake (A), clastic lake (B), wetland (C) and alluvial (D) (described previously in Moreno et al., 2012; González-Sampériz et al., 2013). The VIL sequence exemplifies the characteristic large spatial and temporal variability of facies in shallow lacustrine basins (Cohen, 2003; Valero-Garcés and Moreno, 2011, Valero-Garcés et al., 2014). In this setting, a variety of sub-environments occur from distal alluvial fans (FA D), shallow carbonate ponds with charophyte meadows (FA A), areas with dominant organic deposition (FA C), and other with higher clastic input from the ephemeral or permanent inlets (FA B). Small changes in the hydrology, base level or accommodation space in the basin cause a lateral migration of the sub-environments. Development of a carbonate lake represents higher lake levels than during wetland/peatland stages while alluvial fans prograded over the lake basin during the lowest lake levels phases. Although bathymetric inferences from sediment composition are not straightforward in these settings, clastic lake facies are interpreted as reflecting relatively deep deposition compared to carbonate lake facies as they require higher sediment and water input from the catchment area along small streams and creeks (Valero-Garcés et al., 2014). Examples of modern shallow lake-wetland systems are the Everglades in Florida (USA) or the Ruidera Lakes in Spain. Similar depositional settings have been described during the Quaternary, particularly in the early development stages of large basins such as the Great Salt Lake (Balch et al., 2005) and Titicaca (Fritz et al., 2007).

Seven sedimentary units have been defined in the sequence based on the occurrence of facies association (Fig. 2): Unit VII (74–56m depth) groups facies from a depositional environment characterized as a mosaic of wetlands, peatlands and carbonate lakes with high carbonate production; Unit VI (56–38m depth), contains facies association B (clastic lakes) and C (wetlands); Unit V (38-29m depth) is characterized by the retreat of the wetlands and the progradation of the alluvial fans over the distal areas of the lake basin (FA D and B); Unit IV (29-21m depth) is dominated by distal alluvial fan and mud flat environments (FA D); Unit III (21–15m depth) encompasses clastic lake (FA D) and distal alluvial fan facies (FA C); Unit II (15–3m depth) contains both, clastic and carbonate lake facies associations (A and B); and finally, Unit I (3-0m depth) represents a carbonate lake (FA A) with minor development of wetland/peatland environments (FA C).

3. Methods: a multi-dating technique strategy for an age model

We have applied a number of dating techniques to the VIL sequence, in order to obtain the best possible independent age model: radiocarbon, U/Th series, single-grain quartz OSL, polymineral fine-grain IRSL, paleomagnetism, and (crypto-) tephrochronology (Fig. 2). In the next section we describe for every methodology the sampling procedures (sample numbers, selection criteria, etc.) and the dating technique (chemical procedures, equipment, etc.).

3.1. Radiocarbon (AMS ^{14}C)

A total of twenty three AMS radiocarbon ages were obtained for the VIL sequence (Table 2), twenty of them in the long core VIL05-1B-1T and three from the shorter parallel core VIL05-1A-1L (Aranbarri et al., 2014). Sediment samples were collected as 1 cm-thick sediment slices after detailed macroscopic descriptions and microscopic observation of smear slides to check for terrestrial remains. However, due to the absence of organic terrestrial macro-remains, all the analysed samples correspond to bulk sediment from intervals with relatively high TOC content. Samples were analysed at the Poznan Radiocarbon (Poland) and Beta Analytic (USA) laboratories following their respective protocols for pre-treatment and ages converted into calendar years using the INTCAL13 calibration curve (Reimer et al., 2013).

3.2. U/Th series dating

Eleven samples were selected to run U/Th analyses (Table 3A). Firstly, we looked for pure endogenic inorganic carbonates, but the only occurrence were small carbonate coatings of aquatic plants and Chara fragments. We also selected well-preserved gastropods, although U uptake or loss in biological material poses challenges to dating (Bischoff and Cummins, 2001; Placzek et al., 2006a). Unfortunately, the number of gastropods or biological carbonate coating pieces at discrete levels was never enough to reach the minimum weight (ca. 100 mg) necessary for reliable U/Th analysis by ICP-MS in samples with relatively low U content, and consequently samples from several depths were combined (Table 3). Both biogenic coating carbonate particles and gastropods were cleaned by physically removing any adhered detritus. Samples were then treated with 6% NaOCl for 18–24 h at room temperature to remove all organic material and then washed repeatedly in “ultrapure” water, sonicated for a few minutes to remove adhered solution, washed again, and dried in a vacuum oven overnight at ~70 °C. The chemical procedure used to separate the uranium and thorium was carried out at the University of Minnesota (USA) laboratories following standard methodologies (Edwards et al., 1987; Cheng et al., 2013). Analyses were conducted by inductively coupled plasma mass spectrometry (ICPMS) on a Finnigan-MAT Element equipped with a double focusing sector-field magnet in reversed Nier–Johnson geometry and a single MasCom multiplier from the University of Minnesota laboratories.

Table 1 Summary of sedimentary facies and facies associations in the VIL sequence.

FACIES	Description
SAND	
Grey Sand	Dm to cm thick calcite and silicate sand.
Creamy sand	Cm to dm-thick layers mostly composed of calcite clasts and charophyte remains. Yellowish, brown or white color depending on variable organic, carbonate and silicate contents.
Peaty Sand	Cm-thick, brown carbonate and silicate sand with peat fragments.
Lumaquella	Mm to cm thick, gastropod-rich sand with calcite matrix.
COARSE SILT	
Yellowish silt	Calcite silt with calcite coating, charophyte remains and calcite crystals and intermediate silicate content.
Creamy silt	Calcite silt, dominated by carbonate coating and calcite crystals and lower silicate content than yellowish silt. Variable reddish mottling.
Light grey silt	Calcite and silicate silt with frequent rootlets and grey mottling.
Dark grey silt	Silicate and calcite silt with organic matter and plant remains. Faintly banded. They are the coarsest silt facies.
Peaty silt	Cm thick layers of coarse grey silt with large peat fragments. Abundant mottling.
FINE SILT	
Light grey silt	Silicate and calcite fine silts. Mottling appears in discrete horizons associated to coarser levels with rootlets and plant fragment.
Creamy/white silt	Layers of finer calcite silt, white, more homogeneous, no gastropods. Creamy layers are more massive to faintly banded (cm-scale) coarser calcite silt, with gastropods, larger calcite clasts, charophyte and organic fragments and higher silicate content.
Black and grey silt	Faintly banded, medium size silt dominated by calcite grains (pseudo-oolites, coatings, calcite clasts) and organic fragments. Grey layers are massive to black, mottled with higher silicate content.
Red clayey silt	Dm thick, massive layers of reddish silt dominated by calcite but abundant silicate content and presence of hematite and dolomite.
Laminated grey/greenish silt	Cm to dm-thick layers of calcite and silicate silt.
PEAT	
Massive fine peat	Cm to dm thick, black, massive, homogeneous fine peat.
Coarse peat	Black, massive with coarse peat fragments.
FACIES ASSOCIATIONS	
A. CARBONATE	Sequences composed of creamy and white sands, coarse and fine yellowish silts and organic silts. Minor peat facies. Varied mottling. Depositional environment: littoral charophyte-dominated, carbonate lake. Other intervals with sequences composed of grey sands and grey silts. Depositional environment: littoral carbonate lake with higher clastic input.
B. CLASTIC	Sequences dominated by grey sands, coarse grey silts, fine grey silts and massive, black mottled silts. Alternations of dark and light grey coarse silts, with some fine black mottled silts. In more distal areas, sequences are dominated by finer, laminated silts. Depositional environment: Clastic dominated, higher energy littoral (current and wave influenced) and lower energy sublittoral to distal.
C. WETLAND	Sequences include peat facies (fine and coarse), peaty sands and silts, lumaquellas and organic-rich silts. Some lastic intercalations and carbonate sands. Depositional environment: wetland with some minor carbonate lake.

D. DISTAL ALLUVIAL FAN/MUD FLAT	The sequences are composed of grey, massive to banded silts with frequent mottling and some minor sand layers. Some intervals are dominated by red clayey silts with minor grey silts. Depositional environment: distal alluvial fan associated to mudflat.

3.3. Tephrochronology

To our knowledge, the VIL sequence was one of the first records from NE Spain tested for cryptotephras. Based on a preliminary chronology (Moreno et al., 2012), the 4–24 m depth interval corresponding to ca. 50–159 ka was sampled contiguously and analysed for cryptotephra content. Facies sampled included clay and silt beds with some interspersed fine sandy layers. Numerous techniques have been employed to detect cryptotephra within sedimentary records. These techniques utilise both direct (e.g. extraction of volcanic glass) and indirect (e.g. magnetic signals) approaches. Here the method proposed by Turney et al. (1997), Turney (1998) and Blockley et al. (2005) was employed, involving a stepped density separation using the inert heavy liquid sodium polytungstate (SPT). Firstly a ‘cleaning’ float (specific gravity of 1.98 g cm.^{3}) is performed to remove organics and diatoms, and then an ‘extraction’ float (specific gravity of 2.55 g cm.^{3}) is carried out to separate the tephra shards from the heavier minerogenic material. The published methods are deliberately flexible, allowing the analysed grain-size and the separation densities to be tailored to the host sediment type and expected volcanic ash characteristics. We chose to follow the recommended separation densities, which have been carefully tested by Blockley et al. (2005) to show optimal extraction of the majority of tephra shards encountered within several European volcanic sources (e.g. Icelandic, Italian and Eifel). If present in the VIL core, basaltic glass shards with a higher specific gravity than the SPT extraction density, were not lost, but instead were retained in residues for inspection after the main float was counted. We chose to analyse the sediment fraction between 125 µm and 15 µm. This is a wider size range than the 80 -25 µm fraction most commonly used for cryptotephra (Blockley et al., 2005), reflecting the uncertainty about the volcanic sources able to transport tephra to NE Iberia. Smaller grain-size fractions are commonly used to maximise shard numbers in this way (e.g. Kuehn and Froese, 2010), particularly where sites are very distal from volcanic sources and their typical dispersal axes.

3.4. Single-grain quartz OSL and polymineral fine-grain IRSL

Fourteen luminescence dating samples were collected from unopened sections of the VIL core and from some previously opened sections that had remained wrapped and stored in a cold room since field recovery (Tables 4 and 5). Two luminescence dating techniques have been used on these samples: i) five samples were dated at the Universidad Autónoma de Madrid's commercial dating laboratory using the infrared stimulated luminescence (IRSL) signal from polymineral (mixed mineralogy) fine-grains (i.e. silt-sized grains), and ii) nine samples were dated at the CENIEH laboratories (Burgos, Spain) using the OSL signal from single-grains of quartz. The results of the IRSL study have been already published (Moreno et al., 2012; González- Sampériz et al., 2013) and are only summarised briefly in the current study. The single-grain results were obtained by our own research team as part of the present dating study, and are presented for the first time here. In both cases, the most homogeneous silt or sand-sized layers were sampled in order to minimise uncertainties in gamma dose rate estimation. Blocks of 5–15 cm vertical length were cut from 60 cm-long core sections using a knife and wrapped in light-proof bags for transportation. Coarse-grained (212–250 µm or 180–250 µm) quartz and fine-grained (2–10 µm) polymineral fractions were prepared for OSL and IRSL burial dose estimation, respectively, using standard procedures (Aitken, 1998). A 48% (40 min) hydrofluoric acid (HF) etch was used to remove the alpha-irradiated external layers of the sand-sized quartz grains. The HF-etched quartz fractions were treated with concentrated (30%) hydrochloric acid (1 h duration) to remove any fluoride precipitates, and subsequently re-sieved using a 90 µm sieve to remove any remaining (partially etched) feldspars and smaller disaggregated quartz grains.

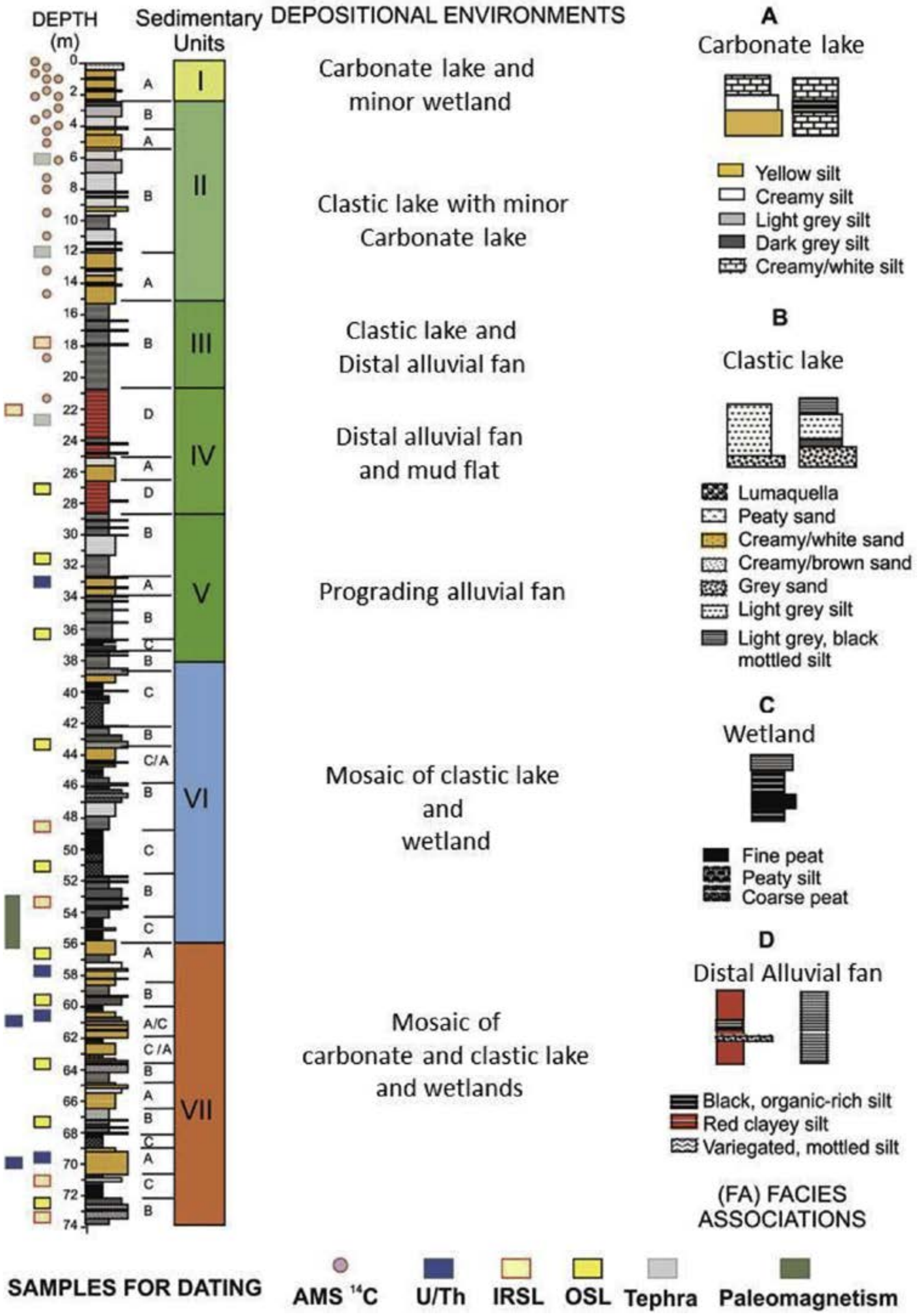

Fig. 2. Stratigraphy of the VIL sequence: sedimentary facies and associations, units, depositional environments and location of samples for different dating methods.

Table 2 Radiocarbon ages for the VIL sequence. Rejected ages are indicated by italics.

Sample	Composite Depth (cm)	Laboratory code	$\delta^{13}C$ (‰)	Radiocarbon age (years BP)	Calibrated age (cal yrs BP) range 2σ
VIL05-1A, 11 cm	11	Beta-332033	27.3	430 ± 30	490 ± 39
VIL05-1A, 132 cm	132	Beta-332034		7460 ± 40	
VIL05-1A, 220 cm	220	Poz-16073		11950 ± 70	
VIL05-1B-1T-2, 2–3 cm	62.5	Beta-319544		2020 ± 30	1974 ± 82
VIL05-1B-1T-2 36-38	96.5	Poz-18451	28.9	3750 ± 40	4084 ± 100
VIL05-1B-1T-3, 6-7	*135*	*Poz-16073*	*32.6*	*11950 ± 70*	*13807 ± 190*
VIL05-1B-1T-3 39-40	173.5	Poz-18509	22.8	7460 ± 50	8279 ± 94
VIL05-1B-1T-4 41-42	233.5	Poz-18453	27.6	9820 ± 50	11248 ± 76
VIL05-1B-1T-5, 55	307.00	Poz-15943		11620 ± 60	13481 ± 174
VIL05-1B-1T-6, 15	*325.4*	*Poz-23667*	*32.7*	*5760 ± 60*	*6543 ± 134*
VIL05-1B-1T-7, 25	*370.4*	*Poz-23669*	*25.3*	*6290 ± 40*	*7237 ± 80*
VIL05-1B-1T-7 55-56.5	*417*	*Poz-18510*	*26.4*	*8200 ± 50*	*9157 ± 143*
VIL05-1B-1T-8 32-35	451.5	Poz-18511	22.4	15390 ± 100	18680 ± 193
VIL05-1B-1T-10, 15	549.5	Poz-15944		18280 ± 110	21844 ± 373
VIL05-1B-1T-12 16-17	*638.2*	*Poz-18454*	*25.7*	*22900 ± 280*	*27584 ± 790*
VIL05-1B-1T-14, 5	734.8	Poz-15945		21020 ± 140	25060 ± 503
VIL05-1B-1T-16, 5	861	Poz-15946		22780 ± 160	27447 ± 570
VIL05-1B-1T-18 13-14	*989.5*	*Poz-18455*	*25.4*	*27000 ± 450*	*31501 ± 840*
VIL05-1B-1T-20, 57	1114.8	Poz-23714	5.9	25520 ± 380	30269 ± 713
VIL05-1B-1T-24, 12	1322.1	Poz-15948		27900 ± 300	32182 ± 755
VIL 05 –1B–1T– 28, 7 cm	1487.7	Poz-17394	12.6	33300 ± 800	38285 ± 1892
VIL 05–1B–1T–35, 44 cm	1912.3	Poz-17287	19.4	36800 ± 800	41589 ± 1348
VIL 05–1B–1T–39, 56 cm	*2177.3*	*Poz-17249*	*29.3*	*22920 ± 360*	*27592 ± 928*

IRSL measurements of the polymineral fine-grain material were made using a Risø TL-DA-10 reader equipped with IR LEDs and a calibrated 90Sr/90Y beta source. Equivalent dose (D_e) estimates were determined from ultraviolet emissions using a multiple aliquot additive dose (MAAD) protocol and a preheat of 180 °C for 10 s prior to an IRSL stimulation for 120 s at 50 °C. Further procedural details for these previously published results are given in the Appendix.

Table 3 U/Th samples for the VIL sequence (A) and obtained results (B).

A)

Sample ID	Sample weight (g)	Sample name	Composite Depth (m)	Sample type
VIL-1	0.0491	VIL05-1B-1T-61, 40-60	28.9	Carbonate coating
VIL-2	0.0209	VIL05-1B-1T-119, 42-49	45.4	gastropods
		VIL05-1B-1T-121, 33-35	45.7	gastropods
VIL-3	0.0261	VIL05-1B-1T-142, 0-10	52.2	gastropods
	0.0216	VIL05-1B-1T-143, 7-11	52.7	gastropods
	0.0429	VIL05-1B-1T-143, 27-30	52.9	gastropods
VIL-4	0.0852	VIL05-1B-1T-144, 0-5	53.1	gastropods
	0.0261	VIL05-1B-1T-144, 20-22	53.2	gastropods
	0.0216	VIL05-1B-1T-144, 25-33	53.3	gastropods
VIL-5	0.0429	VIL05-1B-1T-118, 40	45.1	Carbonate coating
VIL-6	0.0852	VIL05-1B-1T-112, 10-12	43.4	Carbonate coating

B)

Sample	^{238}U		^{232}Th		$\delta^{234}U$		$[^{230}Th/^{238}U]$		$[^{230}Th/^{232}Th]$		Age		Age		$\delta^{234}U_{initial}$	
ID	Ppb		ppt		measured[a]		activity[c]		ppm[d]		uncorrected		corrected [c,e]		corrected[b]	
VIL-1	564	± 1.5	456003	± 7657	957.8	± 4.6	3.91658	± 0.092	79.8	± 2.3	–	–	–	–	–	–
VIL-2	167	± 0.6	90183	± 567	78.8	± 6.4	1.04223	± 0.028	31.8	± 0.9	313,784.7	± 51327.8	299,669.8	± 45407.0	183.8	± 33.3
VIL-3	100	± 0.4	2738	± 29	148.0	± 8.0	1.02330	± 0.014	614.3	± 10.5	216,876.0	± 10444.8	216,246.9	± 10389.0	272.7	± 16.9
VIL-4	111	± 0.5	2276	± 34	104.0	± 8.8	1.04494	± 0.013	840.5	± 16.2	276,135.6	± 19331.9	275,648.7	± 19246.1	226.6	± 23.4
VIL-5	337	± 0.7	464119	± 8122	18.0	± 2.6	1.48947	± 0.102	17.8	± 1.3	–	–	–	–	–	–
VIL-6	190	± 0.4	41233	± 188	2.4	± 2.4	1.16244	± 0.011	88.1	± 0.9	–	–	–	–	–	–

Analytical errors are 2σ of the mean.

[a] $\delta^{234}U = ([^{234}U/^{238}U]_{activity} - 1) \times 1000$.

[b] $\delta^{234}U_{initial}$ corrected was calculated based on ^{230}Th age (T), i.e., $\delta^{234}U_{initial} = \delta^{234}U_{measured}\ X\ e^{\lambda 234 * T}$, and T is corrected age.

[c] $[^{230}Th/^{238}U]_{activity} = 1 - e^{-\lambda 230T} + (\delta^{234}U_{measured}/1000)[\lambda_{230}/(\lambda_{230} - \lambda_{234})](1 - e^{-(\lambda 230 - \lambda 234)\,T})$, where T is the age. Decay constants are 9.1577×10^{-6} yr^{-1} for ^{230}Th, 2.8263×10^{-6} yr^{-1} for ^{234}U, and 1.55125×10^{-10} yr^{-1} for ^{238}U (Cheng et al., 2000).

[d] The degree of detrital ^{230}Th contamination is indicated by the $[^{230}Th/^{232}Th]$ atomic ratio instead of the activity ratio.

[e] Age corrections were calculated using an average crustal $^{230}Th/^{232}Th$ atomic ratio of $4.4 \times 10^{-6} \pm 2.2 \times 10^{-6}$. Those are the values for a material at secular equilibrium, with the crustal $^{232}Th/^{238}U$ value of 3.8. The errors are arbitrarily assumed to be 50%.

Table 4 Dose rate data, multi-grain aliquot additive dose equivalent doses (D_e) and polymineral fine-grain IRSL ages for the VIL samples.

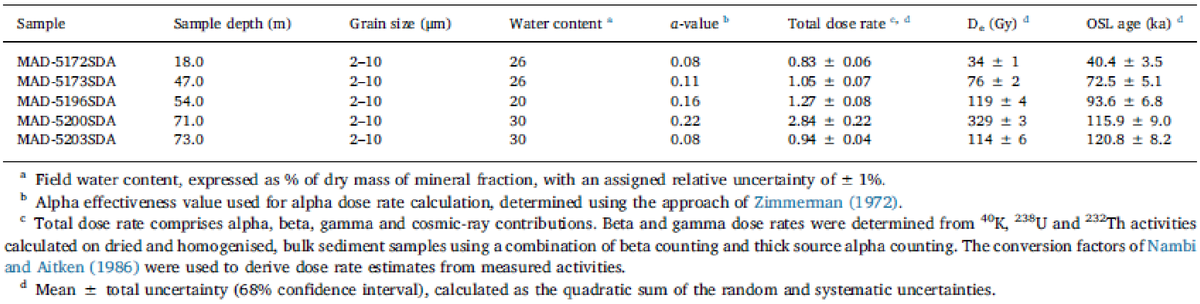

Sample	Sample depth (m)	Grain size (μm)	Water content [a]	a-value [b]	Total dose rate [c, d]	D_e (Gy) [d]	OSL age (ka) [d]
MAD-5172SDA	18.0	2–10	26	0.08	0.83 ± 0.06	34 ± 1	40.4 ± 3.5
MAD-5173SDA	47.0	2–10	26	0.11	1.05 ± 0.07	76 ± 2	72.5 ± 5.1
MAD-5196SDA	54.0	2–10	20	0.16	1.27 ± 0.08	119 ± 4	93.6 ± 6.8
MAD-5200SDA	71.0	2–10	30	0.22	2.84 ± 0.22	329 ± 3	115.9 ± 9.0
MAD-5203SDA	73.0	2–10	30	0.08	0.94 ± 0.04	114 ± 6	120.8 ± 8.2

[a] Field water content, expressed as % of dry mass of mineral fraction, with an assigned relative uncertainty of ± 1%.

[b] Alpha effectiveness value used for alpha dose rate calculation, determined using the approach of Zimmerman (1972).

[c] Total dose rate comprises alpha, beta, gamma and cosmic-ray contributions. Beta and gamma dose rates were determined from ^{40}K, ^{238}U and ^{232}Th activities calculated on dried and homogenised, bulk sediment samples using a combination of beta counting and thick source alpha counting. The conversion factors of Nambi and Aitken (1986) were used to derive dose rate estimates from measured activities.

[d] Mean ± total uncertainty (68% confidence interval), calculated as the quadratic sum of the random and systematic uncertainties.

For the single-grain OSL dating approach applied to coarse-grained quartz, D_e values were estimated from the ultraviolet emissions using the same instrumentation, single-aliquot regenerative-dose (SAR) protocol (Murray and Wintle, 2000), and associated grain rejection criteria described in Arnold et al. (2012, 2013). Specifically, individual grain D_e estimates were rejected from further consideration if they exhibited one or more of the following properties: (i) weak OSL signals (i.e. the net intensity of the natural test-dose signal, T_n, was less than three times the standard deviation of the late-light background signal); (ii) poor recycling ratios (i.e. the ratios of sensitivity-corrected luminescence response (L_x/T_x) for two identical regenerative doses were not consistent with unity at 2σ); (iii) high levels of signal recuperation (i.e. the sensitivity-corrected luminescence response of the 0 Gy regenerative-dose point amounted to more than 5% of the sensitivity-corrected natural signal response (L_n/T_n) at 2σ); (iv) contamination by feldspar grains or inclusions (i.e. the ratio of the L_x/T_x values obtained from two identical regenerative doses measured with and without prior IR stimulation (OSL IR depletion ratio) was less than unity at 2σ); (v) saturated or non-intersecting natural OSL signals (i.e. L_n/T_n values equal to, or greater than, the Imax saturation limit of the dose-response curve); (vi) extrapolated natural OSL signals (i.e. L_n/T_n values lying more than 2s beyond the L_x/T_x value of the largest regenerative-dose administered in the SAR procedure) (vii) anomalous dose-response curves (i.e. those displaying a zero or negative response with increasing dose); or dose-response curves displaying very scattered L_x/T_x values (i.e. those that cannot be successfully fitted with the Monte Carlo procedure and, hence, do not yield finite D_e values and uncertainty ranges).

Single grains were optically stimulated using a focussed 10 mW green (532 nm) laser for 2 s at 125 °C. Sensitivity-corrected dose-response curves were constructed using the first 0.08 s of each green laser stimulation after subtracting a mean background count obtained from the last 0.25 s of the OSL signal. D_e uncertainties were derived from net photon counting statistics, an empirically determined instrument reproducibility of 1.8% per OSL measurement (calculated for the Risø reader used in this study), and a dose-response curve-fitting uncertainty determined using 1000 iterations of the Monte Carlo method described by Duller (2007) (implemented in Analyst v3.24). A preheat of 200 °C for 10 s was used in the SAR procedure prior to measuring the natural- and regenerative-dose OSL signals. A preheat of 160 °C for 10 s was applied prior to each test dose OSL measurement. Single-grain dose-recovery tests performed on V127 yielded measured-to-given dose ratios consistent with unity (0.96 ± 0.03; n =83 D_e values) and a relatively low over-dispersion value of 11 ± 4%, confirming the suitability of the chosen SAR measurement conditions for single-grain D_e estimation.

Environmental dose rates were calculated for the single-grain OSL samples using high-resolution gamma spectrometry measurements made with high-purity Ge detectors (an n-type closed-end coaxial system and a p-type well system) (see SI for further details). To estimate the long-term water content of the single-grain OSL samples we have used the 'as measured' values and included a correction to account for progressive decreases in sediment porosity with time. This correction has been included because of the relatively thick sediment overburden (27–73m) affecting these samples and, hence, the increased likelihood of sediment compaction and dewatering effects with time (e.g., Rendell, 1985; Sheldon and Retallack, 2001; Olley et al., 2004, Kadereit et al., 2012; Lukas et al., 2012; see Tables 1 and SI for further details).

3.5. Paleomagnetism

Due to the fact that the VIL core is not oriented, only the paleomagnetic inclination can be considered (not declination). In addition, it is expected that the paleomagnetic declination is similar for the samples of the same section if the calculated stable paleomagnetic component is primary; i.e., if it is acquired at the time of deposition of the sediments (detrital remanence magnetization DRM). For the last normal chron (Bruhnes chron, ~780 ka, v) up to 5 excursions of the magnetic field occurred (Channell, 2006), and one of them – the Blake excursion ~120 ka -has been recently radiometrically dated in a Northern Spain speleothem between 112 and 116.5 ka (Osete et al., 2012). Consequently, to better constrain the basal age of the VIL sequence, we focused the paleomagnetic study in the interval where the preliminary dating (Moreno et al., 2012) suggested the 120 ka horizon occurs. Thirty-three samples were taken every 10–20 cm along the selected depth interval by cutting the half-core with a ceramic knife into cubes of 2 cm. The analyses were carried out at the Paleomagnetism Laboratory of the University of Burgos, Spain. A 2-G cryogenic instrument with automated alternating field (AF) demagnetization coils were used to measure the remanence and to carry out the stepwise demagnetization procedure, respectively. Three samples were thermally demagnetized but results were good in the AF demagnetization, therefore, the AF demagnetization procedure was preferred. The calculation of the paleomagnetic components was done with Remasoft (Chadima and Hrouda, 2009), which follows the principal component analyses of Kirschvink (1980).

4. Results

4.1. Radiocarbon (AMS ^{14}C)

Seven of the twenty-three AMS ages show reversals or outlier ages compared to the preceding and subsequent samples (in italics in Table 2). The varied admixtures and origin of organic matter in the bulk sediment samples could explain some of these inconsistencies. Three of the samples, at 135, 638.2 and 989.5 cm depth (VIL05-1B-1T) have relatively high algal organic matter content as deduced from their relatively low TOC/TN ratios and δ^{13}C values (Table 2). This feature could explain their relative age overestimates, as they could be more affected by old carbon in the lake water reservoir (Geyh et al., 1998; Hou et al., 2012). The other four ages are inconsistent with the general chronostratigraphy, but there was no clear a priori hypothesis to reject them. We ran an initial Bayesian model (details explained in the Discussion section below) to make the decision on which radiocarbon dates were to be included in the final model and these seven samples giving reversed or outlier ages were excluded. The final age radiocarbon model is therefore constrained by 16 AMS ^{14}C ages for the upper 20 m of the composite sequence.

4.2. U/Th series dating

A number of problems common when dating lacustrine carbonates by U/Th (Placzek et al., 2006a) were encountered in the VIL sequence; finally, only three samples produced ages (VIL-2, -3 and -4; Table 3B). Firstly, even after long procedures, the amount of suitable material collected was too small, thus leading to higher uncertainty in the results. Secondly, carbonate-coatings are more difficult to clean than gastropod samples, and even after a very careful cleaning, the detrital 232Th concentration in all samples was very high. The 230Th/232Th ratio is only above 100 for VIL-3 and VIL-4 (Table 3B). This high detrital thorium content impeded the calculation of a meaningful age for samples VIL-1, VIL-5, and VIL-6 and produced a large associated uncertainty in sample VIL-2.

The uncertainties on the three dated samples (VIL-2, -3 and -4) are high, particularly for sample VIL-2, likely because of the high detrital content and the low sample weight. Potential variability in any assumed initial 230Th/232Th ratio is usually high in lacustrine samples because the proportion of ‘‘siliciclastic Th’’ and ‘‘unsupported Th’’ may not be constant (Placzek et al., 2006b). Therefore, age corrections using a constant initial 230Th/232Th ratio introduce larger errors, as reflected in the inaccuracies of the dated samples VIL-2, -3 and -4. Isochron techniques could probably help to obtain an age for these samples after initial 230Th/232Th ratio determination of the non-carbonate detritus. However, the requirement of obtaining multiple sub-samples with different degrees of contamination at the same core depth (same age) prevents the application of this methodology to the VIL core, particularly as it was difficult collecting sufficient material for just one sample at each depth.

Table 5

Dose rate data, single-grain equivalent doses (D_e) and quartz OSL ages for the VIL samples.

Sample	Sample depth (m)	Grain size (μm)	Measured water content [a]	Compaction-corrected water content [b]	Environmental dose rate (Gy/ka)				Equivalent dose (D_e) data				OSL age (ka) [e, j]
					Beta dose rate [c]	Gamma dose rate [c]	Cosmic dose rate [d]	Total dose rate [e, f]	No. of grains [g]	Overdispersion (%) [h]	Age model [i]	D_e (Gy) [e]	
V49	27.0	180–250	27 ± 7	30 ± 8	1.60 ± 0.08	0.95 ± 0.03	0.05 ± 0.01	2.64 ± 0.21	72/1100	29 ± 4	MAM-4	129 ± 18	49.0 ± 7.9
V58	31.6	212–250	13 ± 3	15 ± 4	0.91 ± 0.05	0.63 ± 0.03	0.04 ± 0.01	1.62 ± 0.10	93/1000	37 ± 4	MAM-4	116 ± 13	71.6 ± 9.4
V67	36.6	212–250	19 ± 5	21 ± 5	1.53 ± 0.08	1.01 ± 0.03	0.04 ± 0.01	2.61 ± 0.17	60/1000	18 ± 6	CAM	191 ± 9	73.2 ± 6.1
V99	51.8	212–250	12 ± 3	14 ± 4	0.85 ± 0.04	0.60 ± 0.02	0.02 ± 0.01	1.51 ± 0.08	75/1000	29 ± 4	MAM-4	128 ± 16	84.6 ± 11.3
V110	56.8	180–250	27 ± 7	35 ± 9	0.91 ± 0.05	0.64 ± 0.03	0.02 ± 0.01	1.60 ± 0.14	71/900	29 ± 4	MAM-4	167 ± 16	104.5 ± 14.1
V117	59.8	212–250	24 ± 6	28 ± 7	0.81 ± 0.05	0.57 ± 0.02	0.02 ± 0.01	1.43 ± 0.11	94/1200	26 ± 3	MAM-4	180 ± 18	126.3 ± 16.2
V127	63.9	212–250	13 ± 3	16 ± 4	1.23 ± 0.06	0.77 ± 0.03	0.02 ± 0.01	2.06 ± 0.12	81/1300	13 ± 3	CAM	264 ± 9	128.1 ± 9.1
V135	67.5	212–250	23 ± 6	28 ± 7	0.95 ± 0.05	0.64 ± 0.03	0.02 ± 0.01	1.64 ± 0.14	63/1000	22 ± 4	CAM	220 ± 10	134.1 ± 12.8
V148	72.7	212–250	14 ± 3	19 ± 5	1.02 ± 0.05	0.66 ± 0.02	0.02 ± 0.01	1.72 ± 0.11	75/1000	22 ± 4	CAM	236 ± 11	137.0 ± 10.9

[a] Field water content, expressed as % of dry mass of mineral fraction, with an assigned relative uncertainty of ± 25%.

[b] Corrected field water contents used to calculate the final OSL ages for these samples. Full details of the procedures used to derive these compaction-correction water contents are provided in the Supplementary Information. This correction has been included because of the relatively thick sediment overburdens affecting these samples and, hence, the increased likelihood of sediment compaction and dewatering effects with time.

[c] Measurements made on dried and powdered samples by high-resolution gamma-ray spectrometry. Specific activities have been converted to dose rates using the conversion factors given in Guérin et al. (2011), making allowance for beta-dose attenuation (Mejdahl, 1979; Brennan, 2003).

[d] Cosmic-ray dose rates were calculated using the approach of Prescott and Hutton (1994) and assigned a relative uncertainty of ± 10%.

[e] Mean ± total uncertainty (68% confidence interval), calculated as the quadratic sum of the random and systematic uncertainties.

[f] Includes an internal dose rate of 0.03 Gy/ka with an assigned relative uncertainty of ± 30%.

[g] Number of D_e measurements that passed the SAR rejection criteria and were used for D_e determination/total number of grains analysed.

[h] The relative spread in the D_e dataset beyond that associated with the measurement uncertainties for individual D_e values, calculated using the central age model (CAM) of Galbraith et al. (1999).

[i] Age model used to calculate the sample-averaged D_e value for each sample. MAM-4 = 4-parameter minimum age model of Galbraith et al. (1999). The MAM-4 has been preferred over the 3-parameter minimum age model (MAM-3) for these single-grain datasets on statistical grounds using the maximum log likelihood (L_{max}) score criterion outlined by Arnold et al. (2009). MAM-4 D_e estimates were calculated after adding, in quadrature, a relative error of 10% to each individual D_e measurement error to approximate the minimum underlying dose overdispersion observed in the single-grain dose-recovery test and in an 'ideal' (well-bleached and unmixed) sedimentary sample from this core (sample V127).

[j] Total uncertainty includes a systematic component of ± 2% associated with laboratory beta-source calibration.

The uppermost age (VIL-2) was rejected because it has the largest error and it is also stratigraphically reversed compared to the other two ages (VIL-3 and VIL-4). Thus, although six samples (endogenic and biogenic carbonates) were prepared and analysed, only two biogenic samples (gastropods) could be considered valid samples. Since these two samples (VIL-3 and VIL-4) were obtained close to the base of the core they could provide a basal age for the sequence, although the ages were much older (240 ka in U/Th) compared to the IRSL dates (140 ka, see below). Biological effects were considered responsible for this discrepancy, as one prerequisite for U/Th dating is a chemically-closed radioactive system, and this is unfortunately rarely the case for biogenic carbonate due to chemical mobility of uranium, particularly during early diagenetic stages (Placzek et al., 2006a,b). Unfortunately, the absence of suitable material impeded the use of the U/Th series techniques to correctly date the VIL sequence. However, the basal age could serve as a maximum limiting age for the sequence.

4.3. Tephrochronology

Cryptotephra studies from Europe and the North Atlantic have shown that small concentrations of volcanic ash can be found over several thousands of km away from their source (Lane et al., 2017), therefore we expected some volcanic ash in El Cañizar de Villarquemado. However, only a few tephra shards (< 5 shards per gram) at two intervals (5.90–6.00 and 12.30–12.50 m depth) were detected under high powered optical microscopic analysis of the extracted residues within the depth interval 4–23m. Despite extensive efforts, however, these could not be replicated at higher 1 cm resolution and thus neither their integrity as primary ash fall layers could be confirmed, nor geochemical analyses carried out (Fig. 4). These results are similar to other recent attempts from paleo-archives across the Iberian Peninsula (Sanabria, Estanya; unpublished data) where no cryptotephra were detected or, samples yielded minimal evidence of tephra input and were insufficient for geochemical analysis.

Tephra occurrences in Late Quaternary Iberian records are rare and seem restricted to Early Holocene volcanic activity in La Garrotxa region, Northeastern Spain (Höbig et al., 2012; Bolòs et al., 2015). Volcanic ash could reach the Iberian Peninsula from several sources: the Azores islands to the west, the Iceland to the north and Massif Central and Italian volcanic systems to the East, all of which were active and generated far-travelled tephra deposits during the last glacial cycle.

The most likely reason that ash from northern and eastern volcanic sources did not reach Iberia is because the atmospheric circulation patterns were dominated by a strong westerly and Northwestern component during the Last Glacial period (Moreno et al., 2005), as they are today (Barry and Chorley, 1992). This essentially blocks atmospheric transport paths required for transport of ash from East to far West. In fact, during the last 2010 Icelandic Eyjafallajökull volcano eruption (Stevenson et al., 2012), only small size volcanic particles were detected in Iberia (Revuelta et al., 2012) and no relevant ash particles deposited.

It is unclear why volcanic ash from the Azores volcanic system, located around 2000 km to the west of El Cañizar de Villarquemado and highly active during the Last Glacial with multiple, caldera-forming eruptions (Moore, 1990), has not been found yet in any Iberian lake sequence. One aspect that deserves further study is the role of precipitation and aridity in tephra deposition dynamics, as periods of higher aridity and varied vegetation cover during the Last Glacial Cycle in Iberia (García-Ruiz et al., 2003; González-Sampériz et al., 2010, 2017; Moreno et al., 2012; Sancho et al., 2018), may have significantly reduced the potential for tephra deposition and preservation.

Another possibility is that grain size of the volcanic particles reaching Iberia may be too small to have been detected with our techniques. Tephra grain size distributions distal to source are controlled by factors including the volume of material ejected during the explosive phase of an eruption, the timing and extent of magma fragmentation, and processes of aeolian fractionation during atmospheric transport. Iberia lies several hundreds of km away from most explosive volcanic regions. The 2010 Eyjafallajökull eruption was less explosive than many Late Quaternary eruptions are believed to have been (Davies et al., 2010; Stevenson et al., 2015), however it provides evidence that some volcanic ash may reach Iberia, but only in very small quantities and size fractions. Within this investigation, 15 µm was the smallest mesh size used, but if most tephra-fall over Iberia falls within a much smaller particle size range, sieves with smaller mesh diameters may need to be employed in future cryptotephra investigations. This has non-trivial implications for both optically identifying tephra at these small sizes and acquiring geochemical data for characterisation, as the smallest electron microprobe beam size currently in use for glass analysis is 3 µm(Haywood, 2012), whilst ~10 µm is more common (Kuehn et al., 2011).

Whilst cryptotephrochronology was not successful in the VIL sequence, it is clear that to establish the absence or presence of non-visible ash layers in other areas of Iberia, requires a more comprehensive assessment of a larger number of Late Quaternary sediment sequences.

4.4. Paleomagnetism

The paleomagnetic results are shown in Fig. 3. Samples demagnetized below 90 mT. The natural remanent magnetization of all samples averages 6.2 10-4 A/m with a standard deviation of 7.6 10-4 A/m (Fig. 3a). In 23 samples out of 33, two stable components can be calculated, one that demagnetized between 2 and 16 mT (3–7 steps), and the component that directs towards the origin (characteristic) and demagnetizes between 10-30 and 40–90mT (4–19 steps) (Fig. 3b–e). These two components can be calculated in the coarser facies (grey silts and brownish sands), but not in the black clays (Fig. 3d). The viscous component groups in a northerly and normal component, probably due to acquisition of the present-day magnetic field during storage. The characteristic component shows normal and reverse polarities in almost all sections (not in 103, 106 and 109 due to low number of samples), but the declination is not similar among the samples from the same section (or antipodal in the case of opposite polarity, Fig. 3f). Therefore, a secondary stable remanent magnetization was acquired after deposition of the sediments, maybe during coring extraction. Diagenetic redox reactions may have also imprinted a secondary polarity as post-sedimentary magnetization can occur (Roberts, 2015 and references therein). This could have been the case for the black clays, with very low NRM and unstable paleomagnetic behaviour, due to the destruction of ferromagnetic minerals by redox reactions in more organic matter-rich sediments.

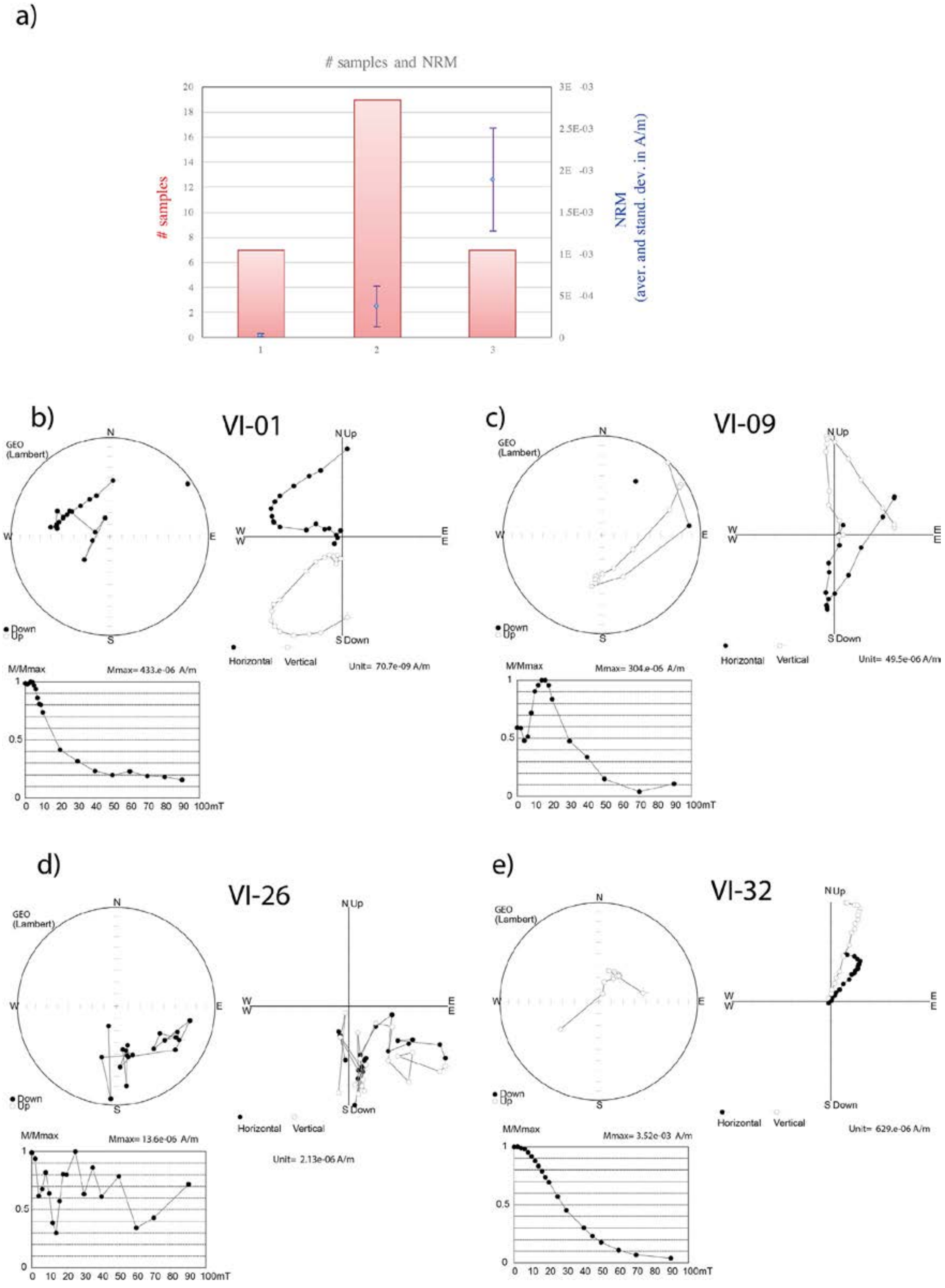

Fig. 3. a) groups of samples and value of NRM (average and standard deviation) in A/m of each group. b to e): stepwise AF demagnetization for selected samples represented in a stereoplot, orthogonal diagram and decay of normalized NRM. Observe that only sample d is from a black clay, with unstable paleomagnetic behaviour. The other three samples show two stable paleomagnetic components. 5. f) Stereographic projection of calculated components. Viscous represent all the components and in pink the average of all together. In the other stereoplots the characteristic component of all samples is represented and in red, the data from the same section (number on top of each stereoplot) is highlighted.

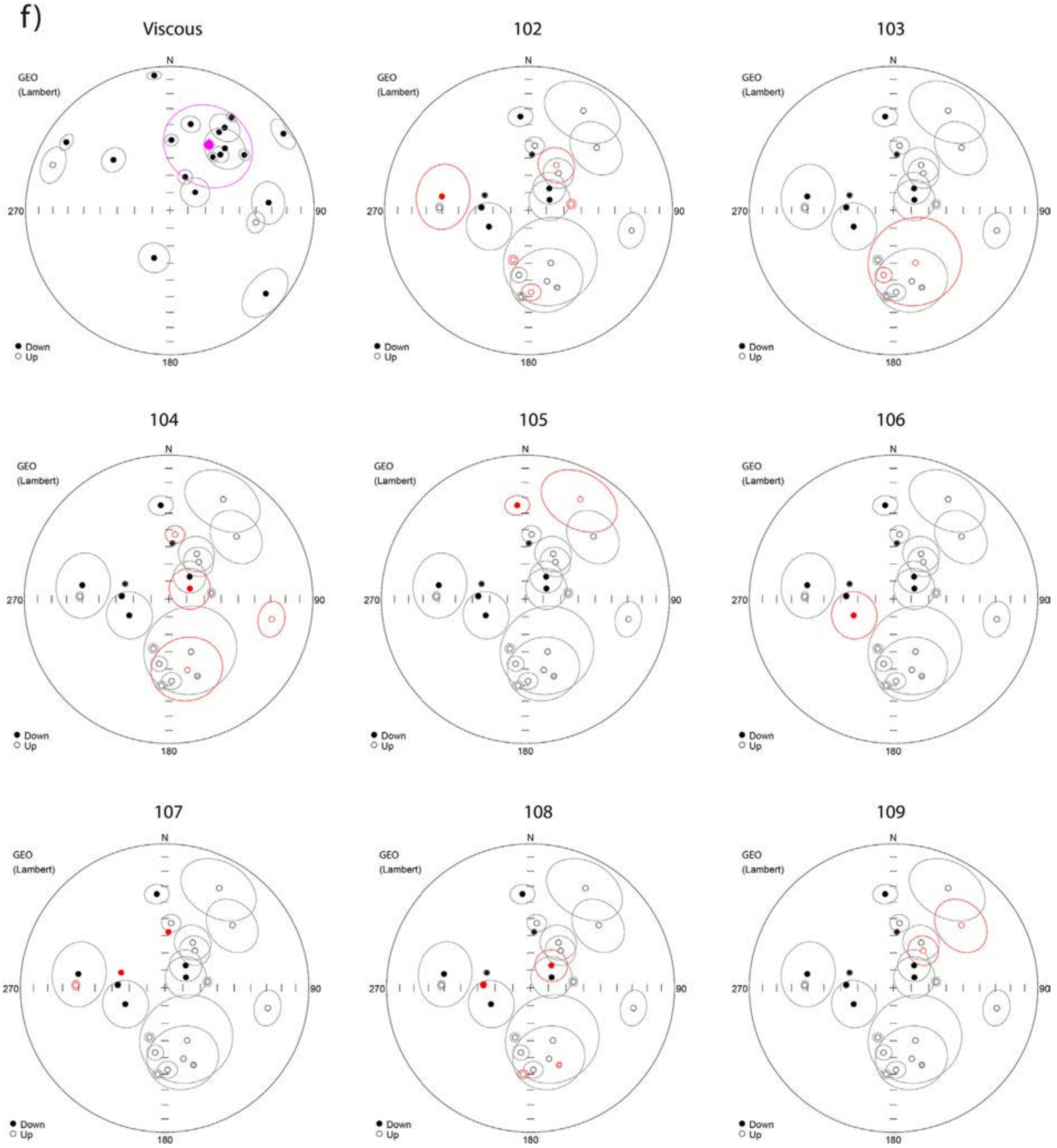

Fig. 3. (continued)

To sum up, paleomagnetic studies could not identify the normal polarity expected for the samples and particularly it was not possible to detect the reverse polarity associated to the Blake excursion (~120 ka) that was anticipated to be found within the lower interval of the sequence. We do not have a valid explanation for this, since at sample level, a stable characteristic magnetic component was calculated (for most samples), but at section level, it was not possible to define local magnetozones.

(a) V127: 300 Gy dose-recovery test

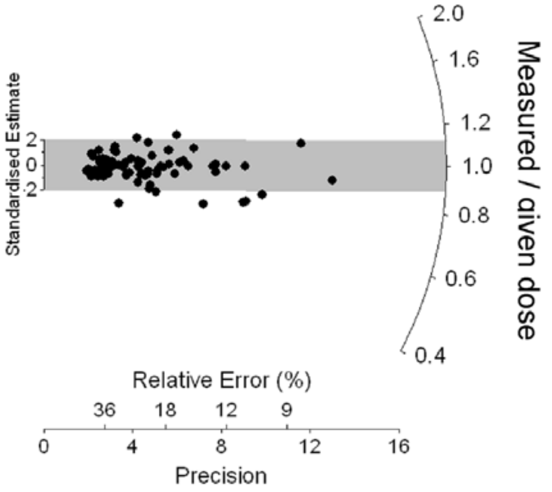

(b) V127: Natural D_e values

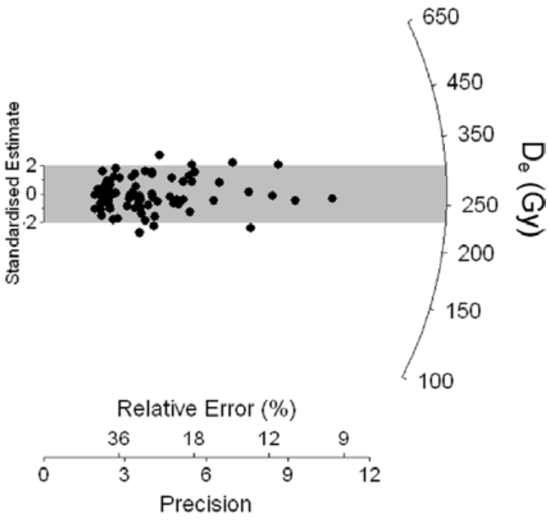

(c) V99: Natural D_e values

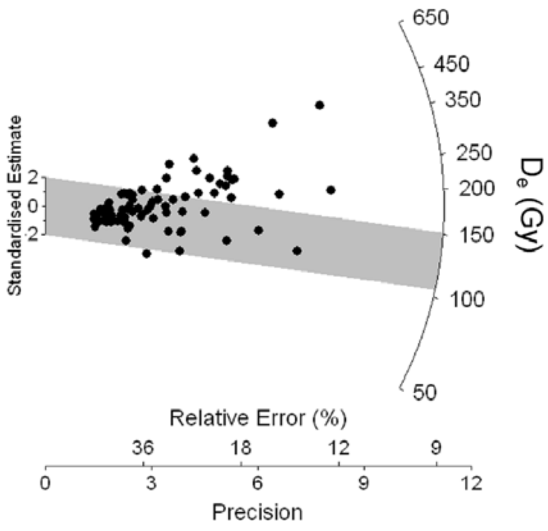

Fig. 4. Representative single-grain D_e distributions for the VIL OSL samples, shown as radial plots. a) Ratios of recovered-to-given dose obtained for individual quartz grains of V127 in the SAR dose-recovery test. The grey shaded region on the radial plot is centred on the administered dose for each grain (sample average = 300 Gy). Individual D_e values that fall within the shaded region are consistent with the administered dose at 2σ. b) Example of a homogeneous D_e distribution with limited dose overdispersion, indicative of a sample that has been sufficiently bleached prior to deposition. Here, the grey band is centred on the weighted mean D_e values used to calculate the OSL age, which was estimated using the central age model of Galbraith et al. (1999).c) Example of a more scattered D_e distribution that is not well-represented by the weighted mean burial dose estimate. This sample is cautiously interpreted as being heterogeneously bleached prior to deposition and its burial dose estimate (indicated by the grey bands) has been derived using the minimum age model of Galbraith et al. (1999).

4.5. Single-grain OSL and polymineral fine-grain IRSL results

4.5.1. Polymineral fine-grain IRSL results

The previously published IRSL ages for the five VIL samples are summarised in Table 4. Multiple aliquot storage tests conducted on a subset of these samples by Universidad Autónoma de Madrid suggest that the polymineral fine-grain IRSL signals may not be significantly affected by anomalous fading; signal losses were reported to be < 3% and within analytical uncertainties following storage times of 240 h (n = 4 aliquots per measurement); though further details of the procedures adopted in these fading assessments are unavailable. Anomalous fading of polymineral IRSL signals has been shown to be a near ubiquitous problem across a wide range of geological provinces (Wintle, 1973; Aitken, 1985, 1998; Huntley and Lamothe, 2001), particularly when employing D_e estimation procedures that include low preheat temperatures (180 °C for 10 s) and measurement of ultraviolet rather than blue IRSL emissions (e.g., Clarke and Rendell, 1997; Preusser, 2003). As such, we cannot preclude the possibility of minor age underestimation arising from unaccounted fading with the polymineral fine-grain IRSL results. It would be worth conducting additional fading tests on these sample using different sized laboratory doses, multiple delay times and signal sensitivity-correction procedures (e.g., Auclair et al., 2003; Huntley and Lamothe, 2001). Irrespective, the polymineral fine-grain IRSL ages are in stratigraphic order and the age of sample MAD-5172SDA (40.4 ± 3.4 ka) is in good agreement with two bracketing AMS ^{14}C ages of 36.3–40.2 ka and 40.2–42.9 ka (Table 5), providing support for the general suitability of the IRSL datasets.

4.5.2. Single-grain quartz OSL results

Table 5 and Fig. 4 summarise the single-grain D_e estimates, dose rate data and final ages obtained for VIL samples. The specific activities of ^{40}K and individual isotopes in the 238U and 232Th series are also shown in Table 6. Isotopic ratios for 226Ra/238U, 210Pb/226Ra and 228Th/228Ra are consistent with unity at 1s or 2s for all nine samples, indicating that the 238U and 232 Th day chains of these sediments are within analytical uncertainty of present-day equilibrium. To calculate the optical ages of these samples, we have assumed that present-day equilibrium in the 238U and 232 Th day chains has prevailed throughout the burial period.

Between 900 and 1300 individual quartz grains were measured per sample (Table 5) and 6–9% of these grains were considered suitable for D_e determination after applying the single-grain quality assurance criteria outlined in Arnold et al. (2013). The vast majority of measured grains were rejected for having weak OSL signals (50–60% of measured grains per sample) and anomalous/scattered dose-response curves (15–30% of measured grains per sample), with the remaining rejection criteria each accounting for less than 5% or 10% of measured grains per sample.

The D_e distributions of these samples can be broadly grouped into two categories. Samples V67, V127, V135 and V148 display homogeneous single-grain D_e distributions, characterised by relatively limited D_e scatter (e.g., Fig. 5b). These D_e datasets are consistent with a single dose population centred on the weighted mean D_e value and display relatively low overdispersion values of ~13–22% (Table 5). These overdispersion values are consistent with the average value of ~20% commonly used to interpret samples as well-bleached and unaffected by post-depositional mixing or significant beta-dose spatial heterogeneity (e.g., Olley et al., 2004; Arnold and Roberts, 2009; Arnold et al., 2011). The overdispersion values of these samples also overlap at 2σ with the over-dispersion value obtained in the single-grain dose-recovery test (11 ± 4%). The consistency of these results suggests that intrinsic sources of D_e scatter captured by the dose-recovery test likely account for the natural D_e distribution characteristics of these four samples, and that extrinsic D_e scatter is relatively unimportant. We have therefore estimated the final burial doses for these samples from their weighted mean D_e estimates, calculated using the central age model (CAM) of Galbraith et al. (1999).

Table 6 High-resolution gamma spectrometry results and daughter-to-parent isotopic ratios for the VIL single-grain OSL samples.

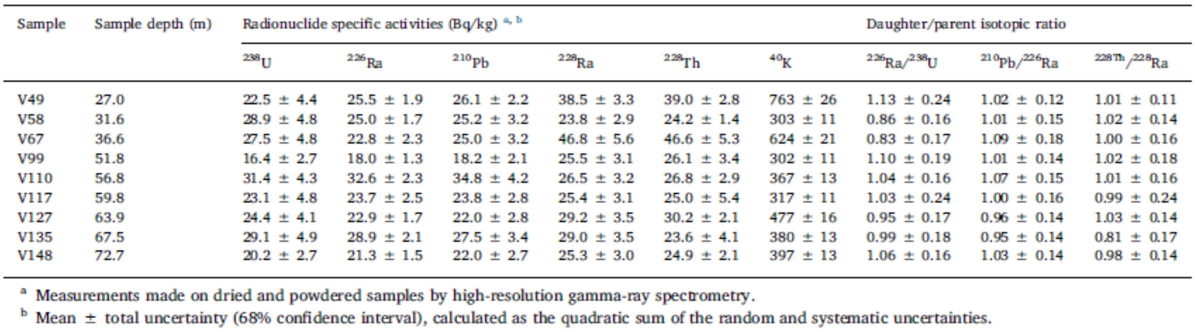

Sample	Sample depth (m)	Radionuclide specific activities (Bq/kg) [a, b]						Daughter/parent isotopic ratio		
		^{238}U	^{226}Ra	^{210}Pb	^{228}Ra	^{228}Th	^{40}K	$^{226}Ra/^{238}U$	$^{210}Pb/^{226}Ra$	$^{228}Th/^{228}Ra$
V49	27.0	22.5 ± 4.4	25.5 ± 1.9	26.1 ± 2.2	38.5 ± 3.3	39.0 ± 2.8	763 ± 26	1.13 ± 0.24	1.02 ± 0.12	1.01 ± 0.11
V58	31.6	28.9 ± 4.8	25.0 ± 1.7	25.2 ± 3.2	23.8 ± 2.9	24.2 ± 1.4	303 ± 11	0.86 ± 0.16	1.01 ± 0.15	1.02 ± 0.14
V67	36.6	27.5 ± 4.8	22.8 ± 2.3	25.0 ± 3.2	46.8 ± 5.6	46.6 ± 5.3	624 ± 21	0.83 ± 0.17	1.09 ± 0.18	1.00 ± 0.16
V99	51.8	16.4 ± 2.7	18.0 ± 1.3	18.2 ± 2.1	25.5 ± 3.1	26.1 ± 3.4	302 ± 11	1.10 ± 0.19	1.01 ± 0.14	1.02 ± 0.18
V110	56.8	31.4 ± 4.3	32.6 ± 2.3	34.8 ± 4.2	26.5 ± 3.2	26.8 ± 2.9	367 ± 13	1.04 ± 0.16	1.07 ± 0.15	1.01 ± 0.16
V117	59.8	23.1 ± 4.8	23.7 ± 2.5	23.8 ± 2.8	25.4 ± 3.1	25.0 ± 5.4	317 ± 11	1.03 ± 0.24	1.00 ± 0.16	0.99 ± 0.24
V127	63.9	24.4 ± 4.1	22.9 ± 1.7	22.0 ± 2.8	29.2 ± 3.5	30.2 ± 2.1	477 ± 16	0.95 ± 0.17	0.96 ± 0.14	1.03 ± 0.14
V135	67.5	29.1 ± 4.9	28.9 ± 2.1	27.5 ± 3.4	29.0 ± 3.5	23.6 ± 4.1	380 ± 13	0.99 ± 0.18	0.95 ± 0.14	0.81 ± 0.17
V148	72.7	20.2 ± 2.7	21.3 ± 1.5	22.0 ± 2.7	25.3 ± 3.0	24.9 ± 2.1	397 ± 13	1.06 ± 0.16	1.03 ± 0.14	0.98 ± 0.14

[a] Measurements made on dried and powdered samples by high-resolution gamma-ray spectrometry.

[b] Mean ± total uncertainty (68% confidence interval), calculated as the quadratic sum of the random and systematic uncertainties.

Samples V49, V58, V99, V110, V117, display broader D_e ranges (e.g., Fig. 5c) and a significant proportion of the individual D_e values are not consistent with the sample-averaged (CAM) burial dose estimates at 2σ. The overdispersion values for these samples range between 26% and 37% and do not overlap at 2σ with the corresponding over-dispersion value obtained for either the single-grain dose-recovery test or the 'best-case scenario' natural D_e distribution observed in the VIL core (i.e., the natural D_e distribution with the lowest overdispersion value in this sample dataset = sample V127: overdispersion = 13 ± 3%), suggesting that dose dispersion originating from extrinsic, field-related sources is more significant. The radial plots also display distinct 'leading-edges' of low D_e values and/or elongated, asymmetric 'tails' of higher D_e values, as has been commonly reported for partially bleached single-grain D_e distributions (e.g., Olley et al., 1999, 2004; Bailey and Arnold, 2006; Arnold et al., 2007, 2009). Taking into account these empirical D_e characteristics, the alluvial and sub-aqueous origin of these deposits, and the potentially limited transportation distances experienced prior to deposition in this closed basin, it seems feasible that the additional D_e scatter may be primarily attributable to insufficient bleaching at the time of deposition; though minor dose dispersion arising from other extrinsic sources of D_e scatter (e.g., beta dose heterogeneity) cannot necessarily be discounted. Post-depositional mixing is not thought to have contributed significantly to the D_e scatter of these samples because primary sedimentary structures and distinctive boundaries are preserved through the sampled region of the core profile. In light of these considerations, the burial doses of samples V49, V58, V99, V110 and V117 have been determined using the 4-parameter minimum age model (MAM-4) of Galbraith et al. (1999). Further support for this choice of age model comes from the accuracy of the MAM-4 OSL age obtained for V49 (49 ± 8 ka). This OSL age is consistent with the expected age range of Unit IV based on an overlying ^{14}C sample (40.2–42.9 ka) and lithostratigraphic correlations of these deposits with MIS 3 (57-29 ka; Lisiecki and Raymo, 2005; Moreno et al., 2012). In contrast, the CAM age for V49 (79 ± 8 ka) is significantly older than the expected age range of Unit IV, consistent with the interpretation that this sample was poorly bleached prior to deposition.

The reliability of the single-grain OSL D_e estimates obtained in this study partly depends on whether the accepted grain populations have sufficiently high dose saturation limits to ensure finite D_e estimation over the true natural burial dose ranges of interest; particularly as the measured D_e values of the Villarquemado samples typically exceed 100 Gy. To examine whether our single-grain OSL D_e results have been compromised by dose saturation, we analysed the characteristic saturation dose (D_0) values of accepted grains for the various coarse-grain quartz samples. Fig. S1 shows the range of single-grain quartz OSL D_0 values obtained for accepted grains from a representative luminescence dating sample (V127); similar trends were observed for all other samples in this study. The weighted mean (CAM) D_0 value for the combined accepted grains of sample V127 (n = 81) is 218 ± 11 Gy (Fig. S1), with the majority of accepted grains (> 80%) exhibiting individual D0 values in excess of 200 Gy. These D_0 values are higher than those typically reported for single-grain quartz OSL datasets (see overview and discussions in Arnold et al., 2016), and sufficiently high to enable finite D_e determination over the empirical burial dose ranges of the Villarquemado samples (Table 5, Fig. 4). As such we do not consider that the single-grain OSL ages have been negatively affected by dose saturation. To explore this issue further, we applied the 2 × D_0 acceptance threshold criterion outlined by Demuro et al. (2015, 2019), which ensures that only grains with 2 × D_0 values higher than a specific burial dose are accepted for final D_e estimation. This additional quality assurance criterion is designed to eliminate grains that produce unrealistically low D_e values purely as a result of insufficient dose saturation limits, thus avoiding potential age underestimation arising from inherently unsuitable grains. Progressively higher 2 × D_0 thresholds of 150–800 Gy (increasing in 50 Gy increments) were applied to all the samples, and the effects on weighted mean D_e were examined after taking into consideration associated 2s uncertainty ranges (see details in Arnold et al., 2016). For all nine single-grain OSL samples, it was found that selecting grains with progressively higher D_0 values did not result in significantly higher CAM D_e values (Fig. S2). Instead, both the CAM D_e and overdispersion remained within 2s of the original values shown in Table 5. These results indicate that the original single-grain OSL ages calculated using all accepted grains have not been adversely affected by OSL dose saturation.

4.5.3. Integration of polymineral fine-grain IRSL and single-grain quartz OSL ages

The nine single-grain OSL ages are internally consistent and in correct stratigraphic order, providing additional support for our age model selection procedure. The single-grain quartz OSL ages and polymineral fine-grain IRSL ages are also in broad agreement with each other at their 1σ or 2σ error ranges, and provide a stratigraphically consistent combined chronological dataset. There are signs of an emergent systematic deviation between the single-grain quartz OSL ages and polymineral fine-grain IRSL ages over the lower 15 m of the core (between a depth range of 59–74 m), though the two chronological datasets remain statistically indistinguishable at 2σ. The general age agreement between the polymineral fine-grain IRSL and single-grain quartz OSL methods is somewhat unexpected for at least some of these samples (i.e., samples V49, V58, V99, V110 and V117) given that they show evidence of prominent single-grain D_e scatter that appears to be related to partial bleaching. The complicating effects of partial bleaching cannot be directly evaluated for the polymineral fine-grain IRSL datasets as the measured aliquots contain 105-106 grains, and therefore give rise to homogenised (grain-averaged) D_e values (e.g., Arnold and Roberts, 2009; Arnold et al., 2013). Any resultant age overestimations associated with such polymineral IRSL averaging effects may not be apparent in the present study if opposing biases have acted to mask the effects of insufficient bleaching (e.g., polymineral IRSL age underestimation related to anomalous fading that has gone undetected in the existing laboratory assessments, or absence of a suitable overburden compaction correction procedure in the previously published IRSL study; see Supplementary Material for discussions of luminescence dating sensitivity to the compaction correction procedure). However, given the apparent agreement of the polymineral IRSL and single-grain OSL ages, and the difficulties of directly demonstrating that the IRSL ages have otherwise been compromised by compensatory biasing effects, we consider both luminescence datasets to be valid for Bayesian age-depth modelling purposes.

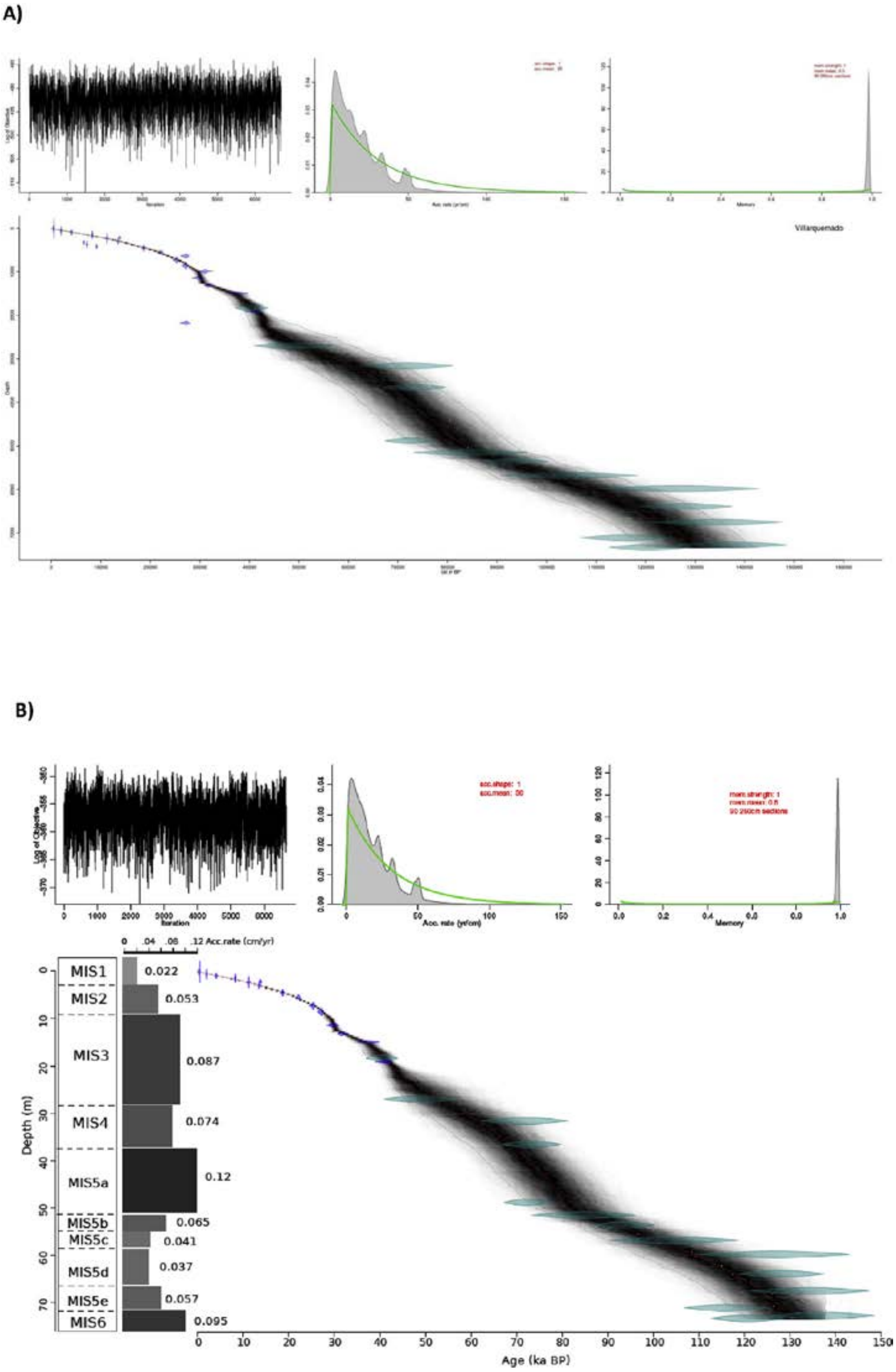

Fig. 5. The Bayesian Age model for the VIL sequence with all the dates included (A) and the final result with the main sedimentation rate changes indicated (B).

That said, we place greater emphasis on single-grain OSL quartz ages generated in the present study because: (i) quartz OSL signals bleach more rapidly than feldspar IRSL signals (e.g., Godfrey-Smith et al., 1988) and therefore offer advantages for some of the deposits that could have experienced limited/filtered bleaching spectra prior to deposition (ii) fast-dominated quartz OSL signals (i.e., those typically isolated with SAR D_e measurement procedures); are not compromised by athermal signal instabilities, unlike many IRSL signals measured at low (50 °C) stimulation temperatures (e.g., Huntley and Lamothe, 2001); (iii) D_e determination at the single-grain scale of analysis circumvents any potentially complicating grain-averaging effects (e.g., Demuro et al., 2008, 2013; Arnold et al., 2012), and enables any subpopulations of poorly bleached grains to be identified and examined with appropriate statistical approaches prior to final age calculation; and (iv) the single-grain quartz OSL ages have been derived using a more thorough consideration of long-term changes in sediment water contents.

5. Discussion

5.1. A Bayesian approach for El Cañizar de Villarquemado age-depth model

5.1.1. Previous chronologies

Since the 2005 core extraction, several attempts have been made at modelling a robust independent chronology for the VIL sequence. The first model included nine AMS ^{14}C ages and five IRSL ages (Moreno et al., 2012). This age model was developed using linear interpolation between all of the radiocarbon and IRSL ages. The base of the sequence was established at ca. 120 ka, with large basal age errors (ca. 10 ka). The robustness of this age model was strengthened by the coherence between the AMS ^{14}C age at 1912 cm (40.2–42.9 ka) and the IRSL age at 1832 cm (40.4 ± 3.4 ka).

A second age model (González-Sampériz et al., 2013) added three more AMS ^{14}C ages (twelve in total) for the top 20 m depth and was constructed following Heegaard et al. (2005). The time resolution for the Holocene improved but remained similar for the previous intervals. According to this second model, the base reached 130 ka and the boundary between MIS 6 and MIS 5 was tentatively located at the base of sedimentary unit VII (74 m depth), while MIS 4 was identified in sedimentary unit V (37-29 m depth) and MIS 3 comprised sedimentary units IV, III and the main part of II (29–5.5 m depth). Sedimentary unit I (top 2.5 m) represented MIS 1. Aranbarri et al. (2014) included four new AMS ^{14}C ages (1 from the long core and three more from the parallel core VIL05-1A) for the Holocene age model.

5.1.2. A Bayesian approach

To build an integrated age model we could only use ages obtained from three of the different techniques originally employed: AMS radiocarbon, IRSL and OSL. As discussed earlier, the only available U/ Th ages were too old, likely as the biogenic carbonate system did not remain chemically closed, and the paleomagnetic studies could not determine a consistent reverse polarity in the lower interval of the sequence that could be related to the Blake excursion (~120 ka). Cryptotephra techniques did not provide suitable material for dating either.

Preliminary age models clearly showed a lack of linearity in the age-depth relationships (Moreno et al., 2012; González-Sampériz et al., 2013; Aranbarri et al., 2014). This is a common feature in terrestrial sequences, where, very often, calibrated radiocarbon ages exhibit non-gaussian probability distributions. Taking into consideration the discussion of the validity of the different data sets from the previous section, we decided to combine the sixteen AMS ^{14}C ages, the five previously published IRSL ages and the nine single-grain OSL ages into a new Bayesian modelling framework (Blockley et al., 2008; Ramsey, 2009; Blaauw and Christen, 2011; Hogg et al., 2011; Goring et al., 2012). The rationale behind this method implies building up a depositional model taking into account the well-known depth (and hence also, by inference, the relative age) relationships between samples used for dating. Of particular significance for lake sequences is the fact that the accumulation process can be modelled by considering that the deposition rate at every depth is a weighted average of the previous depths (Blaauw and Christen, 2011). We have used Bacon v. 2.2 (Blaauw and Christen, 2011) for modelling purposes, which additionally incorporates radiocarbon age calibration using the INTCAL13 curve (Reimer et al., 2013).

Bacon controls core accumulation rates using a gamma autoregressive semi-parametric model with an arbitrary number of subdivisions along the sediment. This implies adding some prior knowledge on the evolution and shape (α) of accumulation rates, which serves as a smoothness factor for the age series, followed by a self-adjusting Markov Chain Monte Carlo (MCMC) process in order to build up a robust-to-outliers age model. The latter involves an adaptive algorithm that learns about the modelled process to automatically tune the MCMC simulation (Blaauw and Christen, 2011). Thus, the model includes as a pre-requisite the known fact that different sections of a sequence have different accumulation rates. This means that low variation in the accumulation rates throughout the deposit implies a high “memory”, or internal dependence amongst sections of the sequence. Therefore, this procedure demands the input of the mean expected accumulation rate (ß) and the prior for the variability of accumulation rate, or “memory”. Additionally, it is necessary to define the number of sections of the core in which the MCMC process will be repeated.

As in most long sequences, we lack precise a priori information on the accumulation rate of the sequence and, given the length of the sequence and the variability in sedimentary facies, building up a chronological model becomes challenging as the sedimentation rate will have certainly changed through the sequence. Therefore, to find the best set of priors to build the most suitable age-depth model for the VIL core, we carried out a sensitivity analysis (see Supplementary material for details on this method). From this analysis our parameters were set as follows: the number of divisions in the VIL sequence was 30, which implies that the MCMC process is roughly renovated every 250 cm and that the variability of the sedimentation process is relatively high (memory strength = 1 and mean correlation of 0.5). We set our prior for the accumulation rate as a gamma distribution with shape 1 (α) and mean 30 (accumulation rate = 30 yr cm^{-1}). The definitive age model for the VIL sequence (Fig. 5) includes thus the 16 available AMS ^{14}C, IRSL and OSL ages, and considers the facies fluctuations along the sequence, especially the changes occurring between sedimentary units VI and V (38 m depth, ca 71 ka BP) and between sedimentary units V and IV (29 m depth, ca. 57 ka BP).

The VIL sequence shows main depositional/vegetational changes and intervals that can concur with the boundaries of the last 6 Marine Isotopic Stages (Shackleton et al., 2002; Lisiecki and Raymo, 2005; Rasmussen et al., 2014). Therefore, according to our age model, we define the following time periods:

- 74–72.3 m depth interval (132,700–130,027 cal yrs BP, corresponding to the end of MIS 6 - 72.3–38.3 m depth (130,027–71,011 cal yrs BP) coincident with MIS 5 - 38.3–29.2 m depth (71,011–57,022 cal yrs BP) concurring with MIS 4
- 29.2–9.9 m depth (57,022–29,007 cal yrs BP) spanning MIS 3
- 9.9–3 m depth (29,007–14,043 cal yrs BP) corresponding to MIS 2
- Upper 3 m depth (14,043 cal yrs BP– current times corresponding to MIS 1

Fig. 5 shows the age – depth model for the VIL sequence. Accumulation rates were higher during cooler periods (end of MIS 6, MIS 5d, MIS5 b, MIS 4, MIS 2 onset and LGM) with average values ranging from 0.095 cm/yr at the end of MIS 6, to 0.053 cm/yr at MIS 2 onset and LGM. However, accumulation rates were also high during MIS 3 when alluvial fans prograded into the lake basin and a more open landscape perhaps also contributed to greater sediment input (Fig. Sed. Rate changes in Supplementary Material). On the contrary, during warm periods such as the Holocene and MIS 5e, the sedimentation rate was much lower (between 0.022 and 0.057 cm/yr) since it was dominated by autochthonous processes (e.g. carbonate productivity in the lake) and a smaller amount of sediment delivery from the catchment.

5.2. The evolution of El Cañizar de Villarquemado lake basin during the last 135,000 years

The new age model allows the definition of the timing for the main environmental and hydrological changes reconstructed in the VIL sequence based on sedimentological, geochemical and palynological indicators in the VIL basin during the last 135 ka (Fig. 6). From a paleohydrological point of view, the development of carbonate lakes in the basin (facies association A in Fig. 2, Table 1) represents periods of higher lake levels than during wetland stages, with higher TOC and lower MS. Alluvial fan deposits, with lower TOC content and higher MS, prograded during the periods with the lowest lake levels in the basin. Additionally, higher hydrophyte and hygrophyte fossil pollen content (aquatic taxa) as well as Pterydophyta spores (ferns), indicate periods of higher lake levels and/or wetland development, thus, increased local moisture conditions in the basin (Fig. 6). Accordingly, increasing percentages in steppe taxa identify arid conditions and lowest lake levels, while fluctuations in the Mediterranean component group are representative of temperature variability.

The age–depth model confirms that carbonate and peat-rich sediments (Fig. 2, Table 1) were mainly deposited during the interglacials (Holocene and MIS 5), but also at the end of MIS 6, the beginning of MIS 4 and a transitional period during the Lateglacial (15–14 ka). During these aforementioned phases, we also find higher proportions of aquatic taxa pointing to increasing local moisture (Fig. 6).

Presence of clastic lacustrine facies, low percentages of Mediterranean taxa and aquatics, and increasing steppe taxa at the bottom of sedimentary unit VII (74–72 m depth, 132,700–129,661 cal yrs BP following our chronological model, thus, end of MIS 6 and beginning of MIS 5), suggest that the base of the sequence corresponds to relatively cooler and drier climate conditions than afterwards. At a global scale, the age of Termination II is considered ca. 132-130 ka (Shackleton et al., 2002; Lisiecki and Raymo, 2005), although it has largely been a matter of debate (see literature review in Helmens, 2014; Martrat et al., 2014; Sier et al., 2015). Similarly, the environmental responses were not synchronous over the European continent (i.e., Woillard and Mook, 1982; Guiot et al., 1989; Tzedakis et al., 1997, 2003; Kukla et al., 1997; Allen and Huntley, 2009).

Based on our age model, the MIS 6 – MIS 5 boundary (ca. 130,027 cal yrs BP) is located at 72.3 m depth although it is at 70.3 m depth (127,566 cal yrs BP) when the first carbonate lake was established (facies association A in Fig. 2). The signature of interglacial conditions in the VIL sequence after the onset of MIS 5 (Fig. 6) was characterized by a trend towards warmer conditions but still relatively low effective moisture, as reflected both in the depositional processes and vegetation responses. This is indicated by the development of a shallow carbonate lake and the lowest proportions of local moisture vegetation formations within MIS 5, and the highest values of steppe taxa (Figs. 2 and 6) with two maximum peaks dated at 128.5 and 127.2 ka BP following our chronological model.

After these maxima, a general decrease in steppe taxa is evidenced since ca. 126.9 ka (MIS 5e). In parallel, local moisture indicators developed in the basin since ca. 125.2 ka. However, the Mediterranean component presents the same values along the MIS 6 – MIS 5 boundary (González-Sampériz et al., 2013; García-Prieto, 2015).

Interestingly, a similar palynological scenario where neither rapid changes nor clear shifts occur regarding regional vegetation (mainly conifers and Mediterranean taxa) has been identified for the Last Termination and the beginning of the Holocene (Aranbarri et al., 2014) (Fig. 6). Thus, the absence of significant changes during the Terminations in this record has been interpreted as a signature of the resilient character of vegetation in Mediterranean continental Iberia (González-Sampériz et al., 2013, 2017; Aranbarri et al., 2014; García-Prieto, 2015).

Detailed facies analyses of the MIS 5 interval in the VIL sequence Units VII and VI, up to 38 m depth and until 70,633 cal yrs BP -show seven major lacustrine carbonate -peat cycles covering the whole of MIS 5. The lacustrine facies are charophyte-rich sand and silt, banded to laminated grey silt, and variegated, bioturbated, mottled carbonate mud and silt (Table 1, Fig. 2). Those cycles are well marked too by TOC-rich intervals 1 to 7 (Fig. 6). The three oldest cycles dated at ca. 129, 125 and 114 ka BP following our chronological model, are dominated mainly by carbonate lake environments in the basin, and suggest deeper lake levels compared to wetland depositional environments. This humid phase in our record corresponds with MIS 5e (ca. 127-112 ka, Fig. 6), in agreement with the most humid period recorded in Monticchio between 127.2 and 109.5 ka, and interpreted as the Eemian by Allen and Huntley (2009). The higher development of carbonate-rich facies in the VIL sequence at this moment would suggest a warmer and more humid Eemian than the Holocene in this region (Aranbarri et al., 2014; García-Prieto, 2015). This is consistent with global patterns of warmer and moister climate conditions of the Eemian (Sánchez-Goñi et al., 1999, 2000; 2005; Tzedakis et al., 2001) and for most reconstructions on mid latitude areas (Van Andel and Tzedakis, 1996; Magri and Tzedakis, 2000; Andersen et al., 2004; Dahl-Jensen et al., 2013; Lunt et al., 2013; Otto-Bliesner et al., 2013; Bakker and Renssen, 2014).

The second half of MIS 5 recorded at VIL is characterized by a larger development of wetlands and less frequent carbonate lake environments, illustrating a trend towards relatively lower humidity (Fig. 2), although pollen indicators show a similar composition of main vegetation groups including large local moisture fluctuations (Fig. 6). Besides the three oldest TOC-rich intervals already mentioned corresponding with MIS 5e, we identify one during MIS 5c (interval number 4, ca 95 ka BP) and the last three (5, 6 and 7, ca 83, 78 and 73 ka PB, respectively, following our age model: Fig. 6) during MIS 5a. Similarly, higher proportions of Mediterranean taxa are also recorded in interstadials MIS 5c and MIS 5a, and interglacial MIS 5e, pointing to higher temperatures (Fig. 6).

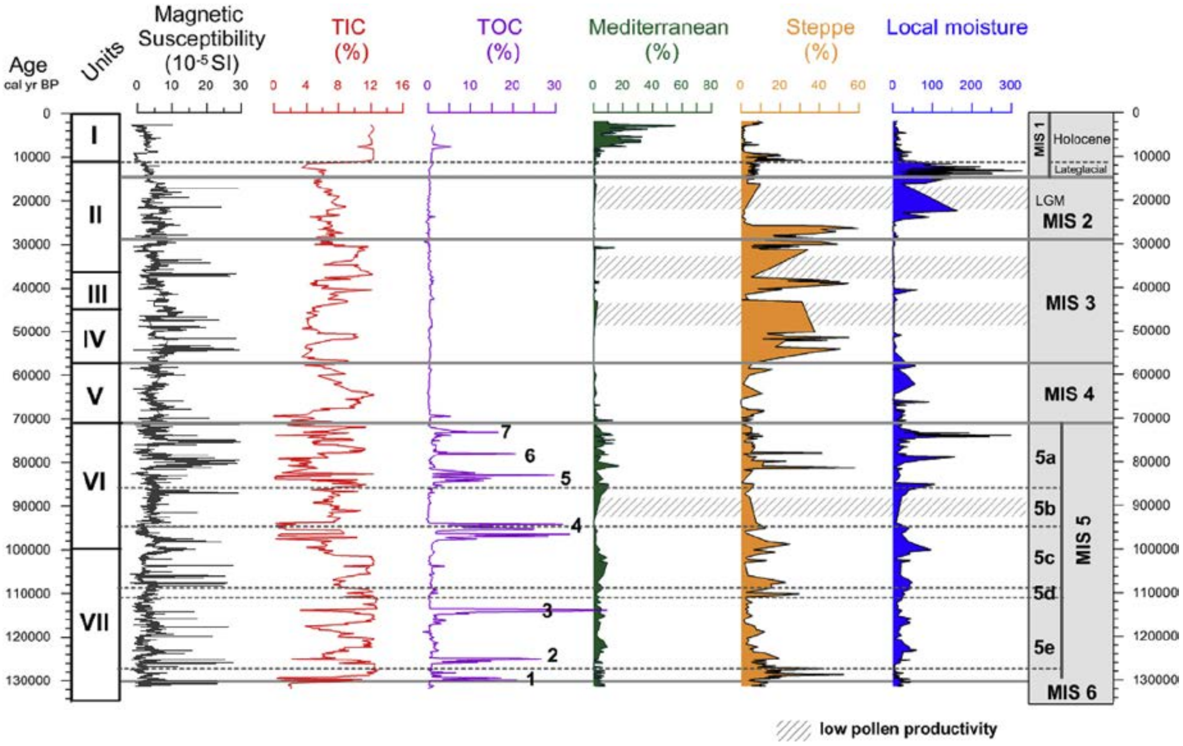

Fig. 6. Main geochemical and palynological data of the VIL sequence plotted in age with both sedimentological units (on the left) and MIS periods (on the right) indicated. Chronological limits for MIS periods follow Lisiecki and Raymo (2005) and Rasmussen et al. (2014) while stadials and interstadials into MIS 5 chronology follow Martrat et al. (2004). Pollen groups are composed by the following taxa: Mediterranean includes evergreen *Quercus, Viburnum, Buxus*, Oleaceae, *Pistacia, Rhamnus, Myrtus*, Thymelaeaceae, *Arbutus unedo*, Cistaceae and *Helianthemum*. Steppe includes *Ephedra distachya* and *E. fragilis* types and Chenopodiaceae. Local moisture is formed by aquatics and Pterydophyta: Cyperaceae, Typhaceae, *Juncus, Sparganium, Thalictrum, Lythrum, Stratiotes, Utricularia, Ledum palustre, Ranunculus, Pedicularis, Myriophyllum, Lemna, Nymphaea, Nuphar, Potamogeton, Isoetes, Alisma, Callitriche, Asplenium*, Monolete, Trilete, *Polypodium, Botrychium, Pteris, Equisetum* and *Selaginella*. Shaded grey bands show intervals with low pollen productivity in MIS 5b, MIS 3 and MIS 2.

The onset of Unit V (38.3 m, 71 ka) witnessed a significant depositional change in the basin, as wetlands started to recede while distal alluvial fans prograded over the central areas of the basin. The Mediterranean taxa disappeared (last peak occurred at 70.4 ka BP following our age model), suggesting colder climate conditions but local moisture pollen indicators still record moderate values

(Fig. 6). Our age model dates this transition as 71 ka corresponding with the onset of MIS 4(Lisiecki and Raymo, 2005). At a regional scale (NE Iberian Peninsula), the transition from MIS 5 to MIS 4 was marked by colder conditions but humidity remained relatively high (González-Sampériz et al., 2010 and references therein), consistent with maximum glacier extension in the northern Iberian mountains (Lewis et al., 2009; Sancho et al., 2018).

In the VIL sequence, the aridity trend that had started during MIS 4 reached a maximum during the lower part of MIS 3 (Unit IV, 29.2–21 m depth, ca. 57,002–44,063 cal yrs BP). During this unit, there is clear evidence for the lowest paleohydrological levels in the basin in the form of red, oxidized, fine silt facies with pedogenic features (facies association D in Fig. 2, Table 1). Strong arid conditions during the whole of MIS 3 (sedimentary units V, IV, III, and the bottom part of unit II: ca. 57-29 ka) are indicated by the highest steppe taxa proportions and the lowest local moisture group percentages of the whole record (Fig. 6). Additionally, two of the four intervals with low pollen productivity or sterility recorded in the VIL sequence (marked by shaded grey bands in Fig. 6) are located in MIS 3, from 50.1-43.1 and from 37.4-31.2 ka BP following our chronological model, and they are the result of low pollen preservation conditions suggesting subaerial exposure.

MIS 2 and the Lateglacial (9.9–3 m depth, ca. 29,007–13,708 cal yrs BP, according to our age model) are characterized by greater environmental and climate variability, as indicated by the diversity of sedimentary facies (Fig. 2). Clastic-dominated lakes and alluvial fans covered the VIL basin, but evidence for subaerial exposure is not found during the first half of MIS 2 (Table 1 and Fig. 2). The LGM is characterized by another new low pollen productivity interval between 4 and 5.5 m depth (22,328–16,085 cal yrs BP from our age model: Fig. 6). Deposition of clastic and carbonate silt facies during the Lateglacial suggest an increase in the flooded area in the VIL basin, and higher run off and sediment delivery. Steppe taxa decreased and never again reached similar proportions to those of MIS 3. Inversely, the aquatic taxa (local moisture group) developed, reaching the maximum values of the whole sequence during the Lateglacial at 13,140 cal yrs BP following our chronological model (Fig. 6). The Mediterranean component slowly expands and only peaks after the first millennia of the Holocene (after 7490 cal yrs BP, Aranbarri et al., 2014).

The Holocene onset at 11.7 ka was abrupt from a sedimentological point of view, with the development of a carbonate lake (Fig. 2), while terrestrial vegetation remained resilient with no significant changes until ca. 9.5 ka (Aranbarri et al., 2014), as observed in other inner Mediterranean regional sequences (González-Sampériz et al., 2017; Morellón et al., 2018 and references therein). Both pollen and sedimentological facies indicate that the most humid Holocene phase occurred between ca. 7.7–5 ka BP and was characterized by the highest development of carbonate facies (Fig. 2, Table 1), the maximum spread of mesophytes, the expansion of mixed Mediterranean oak woodlands with evergreen Quercus as dominant forest communities, and more frequent higher lake level periods (Aranbarri et al., 2014). The return of shallow, carbonate-wetland environments occur in conjunction with a decrease of mesophytes (Aranbarri et al., 2014), consistent with the widely identified increasing aridity of the Late Holocene in the Western Mediterranean (Jalut et al., 2009; Di Rita et al., 2018).

6. Conclusions

A multiple dating technique approach was implemented for the 72 m long VIL sequence, including AMS radiocarbon, IRSL and OSL, U/ Th, tephrochronology and paleomagnetism. In spite of the absence of useful ages from some dating techniques, this type of strategy is essential to maximize the chances of obtaining robust age models in terrestrial sequences. The final Bayesian age model for the VIL sequence includes 16 AMS ^{14}C age, 5 previously published IRSL ages and 9 single-grain OSL ages. We did not find adequate material for some analyses (U/Th, tephrochronology) and other techniques did not provide reliable results (paleomagnetism). The Bayesian approach improved the accuracy and resolution of the age-depth model by incorporating additional information related to the known age relationship between samples, and also related to changes in accumulation rate, as revealed by detailed sedimentological analyses. The age model demonstrates large paleohydrological and vegetation variability since the penultimate Termination, which is consistent with main global climatic trends, despite some local idiosyncrasies derived from stronger continentality in higher altitude Mediterranean areas. Shallow carbonate lake and wetland environments developed during the interglacials (Holocene and MIS 5), but also at the end of MIS 6, the beginning of MIS 4 and the second half of MIS 2 (Lateglacial). Clastic lakes dominated during MIS 2 and MIS 4, and distal alluvial fans prograded over the basin during MIS 3. Sedimentological, geochemical and palynological data suggest that the Eemian was wetter and warmer than the Holocene at VIL. The onset of MIS 4 was marked by cooler temperatures, although conditions remained relatively humid until MIS 3, the most arid interval in the whole sequence. MIS 2 shows large depositional and vegetation variability. The Holocene onset was marked by an abrupt paleohydrological change, but the main terrestrial vegetation change was delayed several millennia until 9.5 ka. This depositional and paleohydrological evolution of the VIL lake during the last interglacial – glacial transition reveals higher moisture variability than expected, an abrupt inception of the last glacial cycle, and a resilient response of vegetation in Mediterranean continental Iberia in both Terminations.

Data availability

Data for this research are available in Mendeley Data Repository.

Acknowledgements

Funding for El Cañizar de Villarquemado sequence research was provided by DINAMO (CGL-BOS 2009–07992), DINAMO2 (CGL-BOS 2012–33063), DINAMO 3 (CGL2015-69160-R) IBERIANPALEOFLORA (CGL-BOS 2012–31717) and GRACCIE-CONSOLIDER (CSD200700067) projects, provided by the Spanish Inter-Ministry Commission of Science and Technology (CICYT) and by the Aragon Government (DGA project, 2005–2006). Tephrochronology research was supported by the UK Natural Environment Research Council consortium RESET (NE/ E015670/1). The single-grain OSL dating research was supported by Australian Research Council (ARC) Future Fellowship project FT130100195 and Discovery Early Career Researcher Award DE160100743. The work of BMB was supported by the IGNEX project (249894), funded by the FRIMEDBIO program of The Research Council of Norway. Graciela Gil-Romera is funded by the DFG project FOR 2358 "Mountain Exile Hypothesis". We are grateful to two anonymous reviewers whose comments and suggestions improved the manuscript.

Appendix A. Supplementary data

Supplementary data to this article can be found online at https://doi.org/10.1016/j.quageo.2019.101006.

References

Aitken, M.J., 1985. Thermoluminescence Dating. Academic Press, London, pp. 359.

Aitken, M.J., 1998. An Introduction to Optical Dating: the Dating of Quaternary Sediments by the Use of Photon-Stimulated Luminescence. Oxford University Press, Oxford, pp. 267.

Allen, J.R.M., Huntley, B., 2009. Last Interglacial palaeovegetation, palaeoenvironments and chronology: a new record from Lago Grande di Monticchio, southern Italy. Quat. Sci. Rev. 28, 1521–1538.

Andersen, K.K., Azuma, N., Barnola, J.M., Bigler, M., Biscaye, P., Caillon, N., Chappellaz, J., Clausen, H.B., Dahl-Jensen, D., Fischer, H., Flückiger, J., 2004. High-resolution record of Northern Hemisphere climate extending into the last interglacial period. Nature 431, 147–151.

Aranbarri, J., González-Sampériz, P., Valero-Garcés, B., Moreno, A., Gil-Romera, G., Sevilla-Callejo, M., García-Prieto, E., Di Rita, F., Mata, M.P., Morellón, M., Magri, D., Rodríguez-Lázaro, J., Carrión, J.S., 2014. Rapid climatic changes and resilient vegetation during the Lateglacial and Holocene in a continental region of south-western Europe. Glob. Planet. Chang. 114, 50–65.

Arnold, L.J., Bailey, R.M., Tucker, G.E., 2007. Statistical treatment of fluvial dose distributions from southern Colorado arroyo deposits. Quat. Geochronol. 2, 162–167.

Arnold, L.J., Roberts, R.G., Macphee, R.D.E., Willerslev, E., Tikhonov, A.N., Brock, F., 2008. Optical dating of perennially frozen deposits associated with preserved ancient plant and animal DNA in north-central Siberia. Quat. Geochronol. 3, 114–136.

Arnold, L.J., Demuro, M., Navazo Ruiz, M., Benito-Calvo, A., Pérez-González, A., 2013. OSL dating of the middle palaeolithic hotel California site, Sierra de Atapuerca, north-central Spain. Boreas 42, 285–305.

Arnold, L.J., Demuro, M., Ruiz, Navazo, 2012. Empirical Insights into multi-grain averaging effects from ‘pseudo’ single-grain OSL measurements. Radiat. Meas. 47, 652–658.

Arnold, L.J., Roberts, R.G., 2009. Stochastic modelling of multi-grain equivalent dose (De) distributions: implications for OSL dating of sediment mixtures. Quat. Geochronol. 4, 204–230.

Arnold, L.J., Roberts, R.G., Galbraith, R.F., DeLong, S.B., 2009. A revised burial dose estimation procedure for optical dating of young and modern-age sediments. Quat. Geochronol. 4, 306–325.

Arnold, L.J., Roberts, R.G., MacPhee, R.D.E., Haile, J.S., Brock, F., Möller, P., Froese, D.G., Tikhonov, A.N., Chivas, A.R., Gilbert, M.T.P., Willerslev, E., 2011. Paper II – dirt, dates and DNA: OSL and radiocarbon chronologies of perennially-frozen sediments and their implications for sedimentary ancient DNA studies. Boreas 40, 417–445.

Arnold, L.J., Demuro, M., Parés, J.M., Pérez-González, A., Arsuaga, J.L., Bermúdez de Castro, J.M., Carbonell, E., 2015. Evaluating the suitability of extended-range luminescence dating techniques over Early and Middle Pleistocene timescales: published datasets and case studies from Atapuerca, Spain. Quat. Int. 389, 167–190.

Arnold, L.J., Duval, M., Demuro, M., Spooner, N.A., Santonja, M., Pérez-González, A., 2016. OSL dating of individual quartz 'supergrains' from the Ancient Middle Palaeolithic site of Cuesta de la Bajada, Spain. Quat. Geochronol. 36, 78–101.

Arnold, L.J., Demuro, M.D., 2018. Dating and optically stimulated luminescence. In: López Varela, S.L. (Ed.), The Encyclopedia of Archaeological Sciences. Wiley-Blackwell, New Jersey, USA, 978-0-470-67461-1, pp. 1992.

Auclair, M., Lamothe, M., Huot, S., 2003. Measurement of anomalous fading for feldspar IRSL using SAR. Radiat. Meas. 37, 487–492.

Bailey, R.M., Arnold, L.J., 2006. Statistical modelling of single grain quartz De distributions and an assessment of procedures for estimating burial dose. Quat. Sci. Rev. 25, 2475–2502.

Bakker, P., Renssen, H., 2014. Last Interglacial model-data mismatch of thermal maximum temperatures partially explained. Clim. Past 10, 1633–1644.

Balch, D., Cohen, A., Schnurrenberger, D., Haskell, B., Valero-Garces, B., Beck, W., Cheng, H., Edwards, L., 2005. Ecosystem and paleohydrological response to Quaternary climate change in the Bonneville Basin, Utah. Palaeogeogr. Palaeoclimatol. Palaeoecol. 221, 99–122.

Barry, R.G., Chorley, R.J., 1992. Atmosphere, Weather and Climate. Routledge, London.

Bischoff, J.L., Cummins, K., 2001. Wisconsin glaciation of the Sierra Nevada (79,000–15,000 yr B.P.) as recorded by rock flour in sediments of Owens lake, California. Quat. Res. 55, 14–24.

Blaauw, M 2012 https://doi.org/10.1016/j.quascirev.2010.11.012.

Blaauw, M., Christen, J.A., 2011. Flexible paleoclimate age-depth models using an autoregressive gamma process. Bayesian Anal. 6, 457–474.

Blockley, S.P.E., Pyne-O'Donnell, S.D.F., Lowe, J.J., Matthews, I.P., Stone, A., Pollard, A.M., Turney, C.S.M., Molyneux, E.G., 2005. A new and less destructive laboratory procedure for the physical separation of distal glass tephra shards from sediments. Quat. Sci. Rev. 24, 1952–1960.

Blockley, S.P.E., Ramsey, C.B., Pyle, D.M., 2008. Improved age modelling and high-precision age estimates of late Quaternary tephras, for accurate palaeoclimate reconstruction. J. Volcanol. Geotherm. Res. 177, 251–262.

Bolòs, X., Martí, J., Becerril, L., Planagumà, L.L., Grosse, P., Barde-Cabusson, S., 2015. Volcano-structural analysis of La Garrotxa volcanic field (NE Iberia): implications for the plumbing system. Tectonophysics 642, 58–70.

Brauer, A., Allen, J.R.M., Mingram, J., Dulski, P., Wulf, S., Huntley, B., 2007. Evidence for last interglacial chronology and environmental change from Southern Europe. Proc. Natl. Acad. Sci. Unit. States Am. 104, 450–455.

Brennan, B.J., 2003. Beta doses to spherical grains. Radiat. Meas. 37, 299–303.

Broecker, W.S., 2000. Abrupt climate change: causal constraints provided by the paleo-climate record. Earth Sci. Rev. 51, 137–154.

Brown, E.T., Werne, J.P., Lozano-García, S., Caballero, M., Ortega-Guerrero, B., Cabral

Cano, E., Valero-Garces, B.L., Schwalb, A., Arciniega-Ceballos, A., 2012. Scientific drilling in the basin of Mexico to evaluate climate history, hydrological resources, and seismic and volcanic hazards. Sci. Drill. 14, 72–75.

Carrión, J.S., Leroy, S., 2010. Iberian floras through time: land of diversity and survival. Rev. Palaeobot. Palynol. 162, 227–230.

Chadima, M., Hrouda, F., 2009. Remasoft 3.0 Paleomagnetic Data Browser and Analyzer. Agico. Inc., Czech Republic.

Channell, J.E.T., 2006. Late brunhes polarity excursions (mono lake, laschamp, Iceland basin and pringle falls) recorded at odp site 919 (Irminger basin). Earth Planet. Sci. Lett. 244, 378–393.

Cheng, H., Edwards, L.R., Hoff, J., Gallup, C.D., Richards, D.A., Asmerom, Y., 2000. The half-lives of uranium-234 and thorium-230. Chem. Geol. 169, 17–33.

Cheng, H., Lawrence Edwards, R., Shen, C.-C., Polyak, V.J., Asmerom, Y., Woodhead, J., Hellstrom, J., Wang, Y., Kong, X., Spötl, C., Wang, X., Calvin Alexander, E., 2013. Improvements in 230Th dating, 230Th and 234U half-life values, and U–Th isotopic measurements by multi-collector inductively coupled plasma mass spectrometry. Earth Planet. Sci. Lett. 371–372, 82–91.

Clarke, M.L., Rendell, H.M., 1997. Infra-red stimulated luminescence spectra of alkali feldspars. Radiat. Meas. 27, 221–236.

Cohen, A., 2003. Paleolimnology. The History and Evolution of Lake Systems. Oxford University Press, pp. 528.

Dahl-Jensen, D., Albert, M.R., Aldahan, A., Azuma, N., Balslev-Clausen, D., Baumgartner, M., Berggren, A.M., Bigler, M., Binder, T., Blunier, T., Bourgeois, J.C., 2013. Eemian interglacial reconstructed from a Greenland folded ice core. Nature 493, 489–494.

Davies, S.M., Larsen, G., Wastegård, S., Turney, C.S.M., Hall, V.A., Coyle, L., Thordarson, T., 2010. Widespread dispersal of Icelandic tephra: how does the Eyjafjöll eruption of 2010 compare to past Icelandic events? J. Quat. Sci. 25, 605–611.

Davies, S.M., 2015. Cryptotephras: the revolution in correlation and precision dating. J. Quat. Sci. 30 (2), 114–130.

de Beaulieu, J.-L., Reille, M., 1989. The transition from temperate phases to stadials in the long Upper Pleistocene sequence from Les Echets (France). Palaeogeogr. Palaeoclimatol. Palaeoecol. 72, 147–159.

De Deckker, P., Arnold, L.J., van der Kaars, S., Bayon, G., Stuut, J.-B., Perner, K., Lopes dos Santos, R., Uemura, R., Demuro, M., 2019. Marine Isotope Stage 4 in Australasia: a full glacial culminating 65,000 years ago – global connections and implications for human dispersal. Quat. Sci. Rev. 204, 187–207.

Demuro, M., Roberts, R.G., Froese, D.G., Arnold, L.J., Brock, F., Bronk Ramsey, C., 2008. Optically stimulated luminescence dating of single and multiple grains of quartz from perennially frozen loess in western Yukon Territory, Canada: comparison with radiocarbon chronologies for the late Pleistocene Dawson tephra. Quat. Geochronol. 3, 346–364.

Demuro, M., Arnold, L.J., Froese, D.G., Roberts, R.G., 2013. OSL dating of loess deposits bracketing Sheep Creek tephra beds, northwest Canada: dim and problematic single-grain OSL characteristics and their effect on multi-grain age estimates. Quat. Geochronol. 15, 67–87.

Demuro, M., Arnold, L.J., Parés, J.M., Sala, R., 2015. Extended-range luminescence chronologies suggest potentially complex bone accumulation histories at the Early-to-

Middle Pleistocene palaeontological site of Huéscar-1 (Guadix-Baza basin, Spain). Quat. Int. 389, 191–212.

Demuro, M., Arnold, L.J., Aranburu, A., Sala, N., Arsuaga, J.-L., 2019. New bracketing luminescence ages constrain the Sima de los Huesos hominin fossils (Atapuerca, Spain) to MIS 12. J. Hum. Evol. 131, 76–95. , Accessed date: 5 December 2018.

Di Rita, F., Fletcher, W.J., Aranbarri, J., Margaritelli, G., Lirer, F., Magri, D., 2018. Holocene forest dynamics in central and western Mediterranean: periodicity, spatio-temporal patterns and climate influence. Sci. Rep. 8, 8929.

Duller, G.A.T., 2007. Assessing the error on equivalent dose estimates derived from single aliquot regenerative dose measurements. Ancient TL 25, 15–24.

Edwards, R.L., Chen, J.H., Wasserburg, G.J., 1987. 238U-234U-230Th-232Th systematics and the precise measurements of time over the past 500.000 years. Earth Planet. Sci. Lett. 81, 175–192.

Fritz, S.C., Baker, P.A., Seltzer, G.O., Ballantyne, A., Tapia, P., Cheng, H., Edwards, R.L., 2007. Quaternary glaciation and hydrologic variation in the South American tropics as reconstructed from the Lake Titicaca drilling project. Quat. Res. 68, 410–420.

Fu, X., Cohen, T.J., Arnold, L.J., 2017. Extending the record of lacustrine phases beyond the last interglacial for Lake Eyre in central Australia using luminescence dating. Quat. Sci. Rev. 162, 88–110.

Galbraith, R.F., Roberts, R.G., Laslett, G.M., Yoshida, H., Olley, J.M., 1999. Optical dating of single and multiple grains of quartz from Jinmium rock shelter, northern Australia: Part I, experimental design and statistical models. Archaeometry 41, 339–364.

García-Prieto, E., 2015. Dinámica paleoambiental durante los últimos 135.000 años en el Alto Jiloca: el registro lacustre de El Cañizar (PhD Thesis). Universidad de Zaragoza, Spain.

García-Ruiz, J.M., Valero-Garcés, B.L., Martí-Bono, C., González-Sampériz, P., 2003. Asynchroneity of maximum glacier advances in the central Spanish Pyrenees. J. Quat. Sci. 18, 61–72.

García-Ruiz, J.M., López-Moreno, J.I., Vicente-Serrano, S., Lasanta-Martínez, T., Beguería, S., 2011. Mediterranean water resources in a global change scenario. Earth Sci. Rev. 105, 121–139.

Geyh, M.A., Schotterer, U., Grosjean, M., 1998. Temporal changes of the ^{14}C reservoir effect in lakes. Radiocarbon 40 (2), 921–931.

Giorgi, F., Lionello, P., 2008. Climate change projections for the Mediterranean region. Glob. Planet. Chang. 63, 90–104.

Godfrey-Smith, D.I., Huntley, D.J., Chen, W.H., 1988. Optical dating studies of quartz and feldspar sediment extracts. Quat. Sci. Rev. 7, 373–380.

González-Sampériz, P., Valero-Garcés, B.L., Moreno, A., Morellón, M., Navas, A., Machín, J., Delgado-Huertas, A., 2008. Vegetation changes and hydrological fluctuations in the Central Ebro Basin (NE Spain) since the Late Glacial period: saline lake records. Palaeogeogr. Palaeoclimatol. Palaeoecol. 259, 157–181.

González-Sampériz, P., Leroy, S.A.G., Carrión, J.S., Fernández, S., García-Antón, M., Gil-

García, M.J., Uzquiano, P., Valero-Garcés, B., Figueiral, I., 2010. Steppes, savannahs, forests and phytodiversity reservoirs during the Pleistocene in the Iberian Peninsula. Rev. Palaeobot. Palynol. 162, 427–457.

González-Sampériz, P., García-Prieto, E., Aranbarri, J., Valero-Garcés, B.L., Moreno, A., Gil-Romera, G., Sevilla-Callejo, M., Santos, L., Morellón, M., Mata, P., Andrade, A., Carrión, J.S., 2013. Reconstrucción paleoambiental del último ciclo glacial en la Iberia continental: la secuencia del Cañizar de Villarquemado (Teruel). Cuadernos de Investigación Geográfica 39, 49–76.

González-Sampériz, P., Aranbarri, J., Pérez-Sanz, A., Gil-Romera, G., Moreno, A., Leunda, M., Sevilla-Callejo, M., Corella, J.P., Morellón, M., Oliva, B., Valero-Garcés, B., 2017. Environmental and climate change in the southern central pyrenees since the last glacial maximum: a view from the lake records. Catena 149, 668–688.

Goring, S.J., Williams, J.W., Blois, J.L., Jackson, S.T., Paciorek, C.J., Booth, R.K., Marlon, J.R., Blaauw, M., Christen, J.A., 2012. Deposition times in the northeastern United States during the Holocene: establishing valid priors for Bayesian age models. Quat. Sci. Rev. 48, 54–60.

Gracia, F.J., Gutiérrez, F., Gutiérrez, M., 2003. The Jiloca karst polje-tectonic graben (Iberian Range, NE Spain). Geomorphology 52, 215–231.

Guérin, G., Mercier, N., Adamiec, G., 2011. Dose-rate conversion factors: update. Ancient TL 29, 5–8.

Guiot, J., Pons, A., deBeaulieu, J.L., Reille, M., 1989. A 140,000-year continental climate reconstruction from two European pollen records. Nature 338, 309–313.

Gutiérrez-Elorza, M., Gracia, F.J., 1997. Environmental interpretation and evolution of the Tertiary erosion surfaces in the Iberian Range (Spain). Geol. Soc. Lond. Spec. Publ. 120, 147–158.

Gutiérrez, F., Gutiérrez-Elorza, M., Gracia, F.J., McCalpin, J.P., Lucha, P., Guerrero, J., 2008. Plio-Quaternary extensional seismotectonics and dreinage natural development in the central sector of the Iberian Chain (NE Spain). Geomorphology 102, 21–42.

Gutiérrez, F., Gracia, F.J., Gutiérrez, M., Lucha, P., Guerrero, J., Carbonel, D., Galve, J.P., 2012. A review on Quaternary tectonic and nontectonic faults in the central sector of the Iberian Chain, NE Spain. J. Iber. Geol. 38 (1), 145–160.

Haywood, C., 2012. High spatial resolution electron probe microanalysis of tephras and melt inclusions without beam-induced chemical modification. Holocene 22 (1), 119–125.

Heegaard, E., Birks, H.J.B., Telford, R.J., 2005. Relationships between calibrated ages and depth in stratigraphical sequences: an estimation procedure by mixed effect regression. Holocene 15, 1–7.

Helmens, K.F., 2014. The last interglacial-glacial cycle (MIS 5-2) re-examined based on long proxy records from central and northern Europe. Quat. Sci. Rev. 86, 115–123.

Höbig, N., Weber, M.E., Kehl, M., Weniger, G.-H., Julià, R., Melles, M., Fülöp, R.-H., Vogel, H., Reicherter, K., 2012. Lake Banyoles (northeastern Spain): a Last Glacial to Holocene multi-proxy study with regard to environmental variability and human occupation. Quat. Int. 274, 205–218.

Hodell, D.A., Anselmetti, F.S., Ariztegui, D., Brenner, M., Curtis, J.H., Gilli, A., Grzesik, D.A., Guilderson, T.J., Mnller, A.D., Bush, M.B., Correa-Metrio, A., Escobar, J., Kutterolf, S., 2008. An 85-ka record of climate change in lowland Central America. Quat. Sci. Rev. 27, 1152–1165.

Hoek, W.Z., Yu, Z.C., Lowe, J.J., 2008. INTegration of ice-core, MArine, and TErrestrial records (INTIMATE): refining the record of the last glacial-interglacial transition. Quat. Sci. Rev. 27, 1–5.

Hogg, A., Palmer, J., Boswijk, G., Turney, C., 2011. High-precision radiocarbon measurements of tree-ring dated wood from New Zealand: 195 BC-AD 995. Radiocarbon 53 (3), 529–542.

Hou, J., D'Andrea, W.J., Liu, Z., 2012. The influence of ^{14}C reservoir age on interpretation of paleolimnological records from the Tibetan Plateau. Quat. Sci. Rev. 48, 67–79.

Huntley, D.J., Lamothe, M., 2001. Ubiquity of anomalous fading in K-feldspars and the measurement and correction for it in optical dating. Can. J. Earth Sci. 38, 1093–1106.

Jalut, G., Dedoubat, J.J., Fontugne, M., Otto, T., 2009. Holocene circum-Mediterranean vegetation changes: climate forcing and human impact. Quat. Int. 200, 4–18.

Kadereit, A., DeWitt, R., Johnson, T.C., 2012. Luminescence properties and optically (post-IR blue-light) stimulated luminescence dating of limnic sediments from northern Lake Malawi – chances and limitations. Quat. Geochronol. 10, 160–166.

Kirschvink, J.L., 1980. The least-squares line and plane and the analysis of paleomagnetic data. Geophys. J. R. Astron. Soc. 62, 669–718.

Kuehn, S.C., Froese, D.G., 2010. Tephra from ice-A Simple method to routinely mount, polish, and quantitatively analyze Sparse fine particles. Microsc. Microanal. 16 (2), 218–225.

Kuehn, S.C., Froese, D.G., Shane, P.A.R., INTAV Intercomparison Participants, 2011. The INTAV intercomparison of electron-beam microanalysis of glass by tephrochronology laboratories: results and recommendations. Quat. Int. 246 (1–2), 19–47.

Kukla, G., McManus, J.F., Rousseau, D.-D., Chuine, I., 1997. How long and stable was the Last Interglacial. Quat. Sci. Rev. 16, 605–612.

Lane, C.S., Lowe, D.J., Blockley, S.P.E., Suzuki, T., Smith, V.C., 2017. Advancing tephrochronology as a global dating tool: applications in volcanology, archaeology, and palaeoclimatic research. Quat. Geochronol. 40, 1–7.

Lézine, A.M., von Grafenstein, U., Andersen, N., Belmecheri, S., Bordon, A., Caron, B., Cazet, J.P., Erlenkeuser, H., Fouache, E., Grenier, C., Huntsman-Mapila, P., Hureau-Mazaudier, D., Manelli, D., Mazaud, A., Robert, C., Sulpizio, R., Tiercelin, J.J., Zanchetta, G., Zeqollari, Z., 2010. Lake Ohrid, Albania, provides an exceptional multi-proxy record of environmental changes during the last glacial–interglacial cycle. Palaeogeogr. Palaeoclimatol. Palaeoecol. 287, 116–127.

Lewis, C., McDonald, E., Sancho, C., Peña, J.L., Rhodes, E., 2009. Climatic implications of correlated Upper Pleistocene glacial and fluvial deposits on the Cinca and Gállego Rivers (NE Spain) based on OSL dating and soil stratigraphy. Glob. Planet. Chang. 67, 141–152.

Lisiecki, L.E., Raymo, M.E., 2005. A Pliocene-Pleistocene stack of 57 globally distributed benthic d18O records. Paleoceanography 20, PA2007.

Litt, T., Krastel, S., Sturm, M., Kipfer, R., Örcen, S., Heumann, G., Franz, S.O., Ülgen, U.B., Niessen, F., 2009. “PALEOVAN”, international continental scientific drilling program (ICDP): site survey results and perspectives. Quat. Sci. Rev. 28, 1555–1567.

Lionello, P., Mallanotte-Rizzoli, P., Boscolo, R. (Eds.), 2012. Mediterranean Climate Variability. Developments in Earth and Environmental Sciences, Elsevier, pp. 421.

Lopez-Martín, F., Cabera, M., Cuadrat, J.M., 2007. Atlas Climático de Aragón. Departamento de Medio Ambiente. Gobierno de Aragón, Zaragoza.

Lukas, S., Preusser, F., Anselmetti, F.S., Tinner, W., 2012. Testing the potential of luminescence dating of high-alpine lake sediments. Quat. Geochronol. 8, 23–32.

Lunt, D.J., Abe-Ouchi, A., Bakker, P., Berger, A., Braconnot, P., Charbit, S., Fischer, N., Herold, N., Jungclaus, J.H., Khon, V.C., Krebs-Kanzow, U., Langebroek, P.M., Lohmann, G., Nisancioglu, K.H., Otto-Bliesner, B.L., Park, W., Pfeiffer, M., Phipps, S.J., Prange, M., Rachmayani, R., Renssen, H., Rosenbloom, N., Schneider, B., Stone, E.J., Takahashi, K., Wei, W., Yin, Q., Zhang, Z.S., 2013. A multi-model assessment of Last Interglacial temperatures. Clim. Past 9, 699–717.

Magri, D., Tzedakis, P.C., 2000. Orbital signatures and long-term vegetation patterns in the Mediterranean. Quat. Int. 73–74, 69–78.

Magri, D., Di Rita, F., Aranbarri, J., Fletcher, W., González-Sampériz, P., 2017. Quaternary disappearance of tree taxa from Southern Europe: timing and trends. Quat. Sci. Rev. 163, 23–55.

Martrat, B., Grimalt, J.O., Lopez-Martinez, C., Cacho, I., Sierro, F.J., Flores, J.A., Zahn, R., Canals, M., Curtis, J.A., Hodell, D.A., 2004. Abrupt temperature changes in the western Mediterranean over the past 250,000 years. Science 306, 1762–1765.

Martrat, B., Jimenez-Amat, P., Zahn, R., Grimalt, J.O., 2014. Similarities and dissimilarities between the last two deglaciations and interglaciations in the North Atlantic region. Quat. Sci. Rev. 99, 122–134.

Mejdahl, V., 1979. Thermoluminescence dating: beta-dose attenuation in quartz grains. Archaeometry 21, 61–72.

Melles, M., Brigham-Grette, J., Minyuk, P.S., Nowaczyk, N.R., Wennrich, V., DeConto, R.M., Anderson, P.M., Andreev, A.A., Coletti, A., Cook, T.L., HaltiaHovi, E., Kukkonen, M., Lozhkin, A.V., Rosen, P., Tarasov, P., Vogel, H., Wagner, B., 2012. 2.8 million years of arctic climate change from Lake El’gygytgyn, NE Russia. Science 337 (6092), 315–320.

Moore, R.B., 1990. Volcanic geology and eruption frequency, São Miguel, Azores. Bull. Volcanol. 52, 602–614.

Morellón, M., Aranbarri, J., Moreno, A., González-Sampériz, P., Valero-Garcés, B.L., 2018. Early Holocene humidity patterns in the Iberian Peninsula reconstructed from lake, pollen and speleothem records. Quat. Sci. Rev. 181, 1–18.

Moreno, A., Cacho, I., Canals, M., Grimalt, J.O., Sanchez-Goni, F., Shackleton, N., Sierro, F.J., 2005. Links between marine and atmospheric processes oscillating on a millennial time-scale. A multi-proxy study of the last 50,000 yr from the Alboran Sea (Western Mediterranean Sea). Quat. Sci. Rev. 24, 1623–1636.

Moreno, A., González-Sampériz, P., Morellón, M., Valero-Garcés, B.L., Fletcher, W.J., 2012. Northern Iberian abrupt climate change dynamics during the last glacial cycle: a view from lacustrine sediments. Quat. Sci. Rev. 36, 139–153.

Murray, A.S., Wintle, A.G., 2000. Luminescence dating of quartz using an improved single-aliquot regenerative-dose procedure. Radiat. Meas. 32, 57–73.

Murray, A.S., Roberts, R.G., 1997. Determining the burial time of single grains of quartz using optically stimulated luminescence. Earth Planet. Sci. Lett. 152, 163–180.

Nambi, K.S.V., Aitken, M.J., 1986. Annual dose conversion factors for TL and ESR dating. Archaeometry 28, 202–205.

Olley, J.M., Caitcheon, G.G., Roberts, R.G., 1999. The origin of dose distribution in fluvial sediments, and the prospect of dating single grains from fluvial deposits using optically stimulated luminescence. Radiat. Meas. 30, 207–217.

Olley, J.M., Pietsch, T., Roberts, R.G., 2004. Optical dating of Holocene sediments from a variety of geomorphic settings using single grains of quartz. Geomorphology 60, 337–358.

Ojala, A.E.K., Francus, P., Zolitschka, B., Besonen, M., Lamoureux, S.F., 2012. Characteristics of sedimentary varve chronologies e a review. Quat. Sci. Rev. 43, 45–60.

Osete, M.L., Martín-Chivelet, J., Rossi, C., Edwards, R.L., Egli, R., Muñoz-García, M.B., Wang, X., Pavón-Carrasco, F.J., Heller, F., 2012. The Blake geomagnetic excursion recorded in a radiometrically dated speleothem. Earth Planet. Sci. Lett. 353, 173–181.

Otto-Bliesner, B., Rosenbloom, N., Stone, E., McKay, N.P., Lunt, D.J., Brady, E.C., Overpeck, J.T., 2013. How warm was the Last Interglacial? New model-data comparisons. Philos. Trans. Ser. A Math. Phys. Eng. Sci. 371, 20130097.

Pérez-Mejías, C., Moreno, A., Sancho, C., Bartolomé, M., Stoll, H., Cacho, I., Cheng, H., Edwards, R.L., 2017. Abrupt climate changes during termination III in southern Europe. Proc. Natl. Acad. Sci. U.S.A. 114, 10047–10052.

Placzek, C., Patchett, P.J., Quade, J., Wagner, J.D.M., 2006a. Strategies for successful U-Th dating of paleolake carbonates: an example from the Bolivian Altiplano. Geochem. Geophys. Geosyst. 7, Q05024.

Placzek, C., Quade, J., Patchett, P.J., 2006b. Geochronology and stratigraphy of late Pleistocene lake cycles on the southern Bolivian Altiplano: implications for causes of tropical climate change. Geol. Soc. Am. Bull. 118, 515–532.

Prescott, J.R., Hutton, J.T., 1994. Cosmic ray contribution to dose rates for luminescence and ESR dating: large depths and long-term time variations. Radiat. Meas. 23, 497–500.

Preusser, F., 2003. IRSL dating of K-rich feldspars using the SAR protocol: comparison with independent age control. Ancient TL 21, 17–23.

Ramsey, C.B., 2009. Bayesian analysis of radiocarbon dates. Radiocarbon 51 (1), 337–360.

Rasmussen, S.O., Bigler, M., Blockley, S.P., Blunier, T., Buchardt, S.L., Clausen, H.B., Cvijanovic, I., Dahl-Jensen, D., Johnsen, S.J., Fischer, H., Gkinis, V., Guillevic, M., Hoek, W.Z., Lowe, J.J., Pedro, J.B., Popp, T., Seierstadt, I.K., Steffensen, J.P., Svensson, A.M., Vallelonga, P., Vinther, B.M., Walker, M.J.C., Wheatley, J.J., Winstrup, M., 2014. A stratigraphic framework for abrupt climate changes during the Last Glacial period based on three synchronized Greenland ice-core records: refining and extending the INTIMATE event stratigraphy. Quat. Sci. Rev. 106, 14–28.

Reille, M., de Beaulieu, J.-L., Svobodova, H., Andrieu-Ponel, V., Goeury, C., 2000. Pollen analytical biostratigraphy of the last five climatic cycles from a long continental sequence from the Velay region (Massif Central, France). J. Quat. Sci. 15, 665–685.

Reimer, P.J., Baillie, M.G.L., Bard, E., Bayliss, A., Beck, J.W., Bertrand, C.J.H., Blackwell, P.G., Buck, C.E., Burr, G.S., Cutler, K.B., Damon, P.E., Edwards, R.L., Fairbanks, R.G., Friedrich, M., Guilderson, T.P., Hogg, A.G., Hughen, K.A., Kromer, B., McCormac, G., Manning, S., Bronk Ramsey, C., Reimer, R.W., Remmele, S., Southon, J.R., Stuiver, M., Talamo, S., Taylor, F.W., van der Plicht, J., Weyhenmeyer, C.E., 2004. IntCal04 terrestrial radiocarbon age calibration, 0-26 cal kyr. Radiocarbon 46 (3), 1029–1058.

Reimer, P.J., Baillie, M.G.L., Bard, E., Bayliss, A., Beck, J.W., Blackwell, P.G., Bronk Ramsey, C., Buck, C.E., Burr, G.S., Edwards, R.L., Friedrich, M., Grootes, P.M., Guilderson, T.P., Hajdas, I., Heaton, T.J., Hogg, A.G., Hughen, K.A., Kaiser, K.F., Kromer, B., McCormac, F.G., Manning, S.W., Reimer, R.W., Richards, D.A., Southon, J.R., Talamo, S., Turney, C.S.M., van der Plicht, J., Weyhenmeyer, C.E., 2009. IntCal09 and Marine09 radiocarbon age calibration curves, 0-50,000 years cal. Radiocarbon 51, 1111–1150.

Reimer, P.J., Bard, E., Bayliss, A., Beck, J.W., Blackwell, P.G., Bronk Ramsey, C., Buck, C.E., Cheng, H., Edwards, R.L., Friedrich, M., Grootes, P.M., Guilderson, T.P., Haflidason, H., Hajdas, I., Hatte, C., Heaton, T.J., Hoffmann, D.L., Hogg, A.G., Hughen, K.A., Kaiser, K.F., Kromer, B., Manning, S.W., Niu, M., Reimer, R.W., Richards, D.A., Scott, E.M., Southon, J.R., Staff, R.A., Turney, C.S.M., van der Plicht, J., 2013. IntCal 13 and Marine 13 radiocarbon age calibration curves 0-50,000 years cal. Radiocarbon 55, 1869–1887.

Rendell, H.M., 1985. The precision of water content estimates in the thermoluminescence dating of loess from northern Pakistan. Nucl. Tracks Radiat. Meas. 10, 763–768.

Revuelta, M.A., Sastre, M., Fernández, A.J., Martin, L., Gómez-Moreno, F.J., Artinano, B., Pujadas, M., Molero, F., 2012. Characterization of the Eyjafjallajökull volcanic plume over the Iberian Peninsula by lidar remote sensing and ground-level data collection. Atmos. Environ. 48, 46–55.

Roberts, A.P., 2008. Geomagnetic excursions: knowns and unknowns. Geophys. Res. Lett. 35, L17307. https://doi.org/10.1029/2008GL034719.

Roberts, A.P., 2015. Magnetic mineral diagenesis. Earth Sci. Rev. 151, 1–47.

Rodbell, D.T., Abbott, M.B., 2012. Workshop on drilling of Lake Junin, Peru: potential for development of a continuous tropical climate record. Sci. Drill. 13, 58–60.

Rubio, J.C., 2004. Contexto hidrogeológico e histórico de los humedales del Cañizar. Consejo de la Protección de la Naturaleza de Aragón, Serie de Investigración, Zaragoza.

Rubio, J.C., Simon, J.L., 2007. Tectonic subsidence v, erosional lowering in a controversial intramontane depression: the Jiloca basin (Iberian Chain, Spain). Geol. Mag. 144, 127–141.

Russell, J.M., Bijaksana, S., Vogel, H., Melles, M., Kallmeyer, J., Ariztegui, D., Crowe, S.A., Fajar, S.J., Hafidz, A., Haffner, D., Hasberg, A.K.M., Ivory, S.J., Kelly, C., King, J.W., Kirana, K.H., Morlock, M.A., Noren, A., O'Grady, R., Ordonez, L., Stevenson, J., 2016. The towuti drilling project: paleoenvironments, biological evolution, and geomicrobiology of a Tropical Pacific Lake. Sci. Drill. 21, 29–40.

Sánchez-Goñi, M.F., Eynaud, F., Turon, J.L., Shackleton, N.J., 1999. High resolution palynological record off the Iberian margin: direct land–sea correlation for the last interglacial complex. Earth Planet. Sci. Lett. 171, 123–137.

Sánchez-Goñi, M.F., Turon, J.L., Eynaud, F., Gendreau, S., 2000. European climatic response to millennial-scale changes in the atmosphere-ocean system during the Last Glacial period. Quat. Res. 54, 394–403.

Sánchez-Goñi, M.F., Loutre, M.F., Crucifix, M., Peyron, O., Santos, L., Duprat, J., Malaizé, B., Turon, J.L., Peypouquet, J.P., 2005. Increasing vegetation and climate gradient in Western Europe over the Last Glacial Inception (122–110 ka): data-model comparison. Earth Planet. Sci. Lett. 231 (1–2), 111–130.

Sancho, C., Arenas, C., Pardo, G., Peña-Monné, J.L., Rhodes, E.J., Bartolomé, M., García-Ruiz, J.M., Martí-Bono, C., 2018. Glaciolacustrine deposits formed in an ice-dammed tributary valley in the south-central Pyrenees: new evidence for late Pleistocene climate. Sediment. Geol. 366, 47–66.

Schnurrenberger, D., Russell, J., Kelts, K., 2003. Classification of lacustrine sediments based on sedimentary components. J. Paleolimnol. 29, 141–154.

Shackleton, N.J., Chapman, M., Sánchez-Goñi, M.F., Pailler, D., Lancelot, Y., 2002. The classic marine isotope substage 5e. Quat. Res. 58, 14–16.

Sheldon, N.D., Retallack, G.J., 2001. Equation for compaction of paleosols due to burial. Geology 29, 247–250.

Sier, M.J., Peeters, J., Dekkers, M.J., Pares, J.M., Chang, L., Busschers, F.S.B., Cohen, K.M., Wallinga, J., Bunnik, F.P., Roebroeks, W., 2015. The Blake Event recorded near the Eemian Type locality e a diachronic onset of the Eemian in Europe. Quat. Geochronol. 28, 12–28.

Stein, M., Ben-Avraham, Z., Goldstein, S., Agnon, A., Ariztegui, D., Brauer, A., Haug, G., Ito, E., Yasuda, Y., 2011. Deep drilling at the Dead Sea. Sci. Drill. 46–47.

Stevenson, J.A., Loughlin, S., Rae, C., Thordarson, T., Milodowski, A.E., Gilbert, J.S., Harangi, S., Lukács, R., Højgaard, B., Árting, U., Pyne-O'Donnell, S., MacLeod, A., Whitney, B., Cassidy, M., 2012. Distal deposition of tephra from the Eyjafjallajökull 2010 summit eruption. J. Geophys. Res. 117 B00C10.

Stevenson, J.A., Millington, S.C., Beckett, F.M., Swindles, G.T., Thordarson, T., 2015. Big grains go far: understanding the discrepancy between tephrochronology and satellite infrared measurements of volcanic ash. Atmos. Measur. Tech. 8, 2069–2091.

Turney, C.S.M., 1998. Extraction of rhyolitic component of Vedde microtephra from minerogenic lake sediments. J. Paleolimnol. 19 (2), 199–206.

Turney, C.S.M., Harkness, D.D., Lowe, J.J., 1997. The use of microtephra horizons to correlate Late-glacial lake sediment successions in Scotland. J. Quat. Sci. 12 (6), 525–531.

Tzedakis, P.C., Andrieu, V., de Beaulieu, J.-L., Crowhurst, S., Follieri, M., Hooghiemstra, H., Magri, D., Reille, M., Sadori, L., Shackleton, N.J., Wijmstra, T.A., 1997. Comparison of terrestrial and marine records of changing climate of the last 500,000 years. Earth Planet. Sci. Lett. 150, 171–176.

Tzedakis, P.C., Andrieu, V., Birks, H.J.B., de Beaulieu, J.-L., Crowhurst, S., Follieri, M., Hooghiemstra, H., Magri, D., Reille, M., Sadori, L., Shackleton, N.J., Wijmstra, T.A., 2001. Establishing a terrestrial chronological framework as a basis for biostrati-graphical comparisons. Quat. Sci. Rev. 20, 1583–1592.

Tzedakis, P.C., Frogley, M.R., Heaton, T.H.E., 2003. Last Interglacial conditions in southern Europe, evidence from Ioannina, northwest Greece. Glob. Planet. Chang. 36, 157–170.

Tzedakis, P.C., Hooghiemstra, H., Pälike, H., 2006. The last 1.35 million years at Tenaghi Philippon, revised chronostratigraphy and long-term vegetation trends. Quat. Sci. Rev. 25, 3416–3430.

Tzedakis, P.C., 2007. Seven ambiguities in the Mediterranean palaeoenvironmental narrative. Quat. Sci. Rev. 26, 2042–2066.

Valero-Garcés, B., Moreno, A., 2011. Iberian lacustrine sediment records: responses to past and recent global changes in the Mediterranean region. J. Paleolimnol. 46, 319–325.

Valero-Garcés, B., Morellón, M., Moreno, A., Corella, P., Martín-Puertas, C., Barreiro, F., Pérez, A., Giralt, S., Mata-Campo, M.P., 2014. The carbonate factory in karst lakes: sources, processes and depositional environments in Quaternary Iberian Lakes. Sediment. Geol. 299, 1–29.

Van Andel, T.H., Tzedakis, P.C., 1996. Paleolithic landscapes of Europe and environs, 150,000-25,000 years ago: an overview. Quat. Sci. Rev. 15, 481–500.

Wang, Y.J., Cheng, H., Edwards, R.L., An, Z.S., Wu, J.Y., Shen, C.C., Dorale, J.A., 2001. A high-resolution absolute-dated Late Pleistocene monsoon record from Hulu Cave, China. Science 294, 2345–2348.

Wintle, A.G., 1973. Anomalous fading of thermo-luminescence in mineral samples. Nature 245, 143–144.

Woillard, G.M., 1978. Grande Pile peat bog: a continuous pollen record for the last 140,000 years. Quat. Res. 9 (1), 1–21.

Woillard, G.M., Mook, W.G., 1982. Carbon-14 dates at Grande Pile: correlation of land and sea chronologies. Science 215, 159–161.

Zanchetta, G., Sulpizio, R., Roberts, N., Cioni, R., Eastwood, W.J., Siani, G., Caron, B., Paterne, M., Santacroce, R., 2011. Tephrostratigraphy, chronology and climatic events of the Mediterranean basin during the Holocene: an overview. Holocene 21 (1), 33–52.

Zanchetta, G., Regattieri, E., Giaccio, B., Wagner, B., Sulpizio, R., Francke, A., Vogel, L.H., Sadori, L., Masi, A., Sinopoli, G., Lacey, J.H., Leng, M.L., Leicher, N., 2016. Aligning MIS5 proxy records from Lake Ohrid (FYROM) with independently dated Mediterranean archives: implications for core chronology. Biogeosciences 13, 2757–2768.

Zimmerman, D.W., 1972. Relative thermoluminescence effects of alpha-and beta-irradiation. Radiat. Eff. 14, 81–92.

Zolitschka, B., Anselmetti, F., Ariztegui, D., Corbella, H., Francus, P., Lücke, A., Maidana, N.I., Ohlendorf, C., Schäbitz, F., Wastegård, S., 2013. Environment and climate of the last 51,000 years – new insights from the Potrok Aike maar lake Sediment Archive Drilling project (PASADO). Quat. Sci. Rev. 71, 1–12.